RICE UNIVERSITY

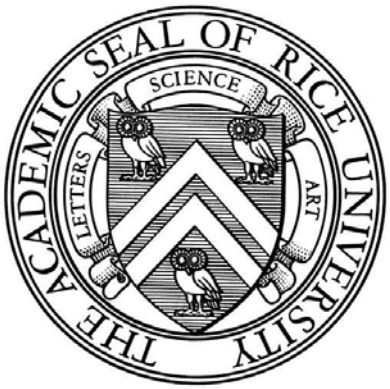

ELECTRON TRANSPORT IN FERROMAGNETIC NANOSTRUCTURES

by
Sungbae Lee

DOCTOR OF PHILOSOPHY

HOUSTON, TEXAS
November, 2007

RICE UNIVERSITY

Electron Transport in Ferromagnetic Nanostructures

by

Sungbae Lee

A THESIS SUBMITTED
IN PARTIAL FULFILLMENT OF THE
REQUIREMENTS FOR THE DEGREE

Doctor of Philosophy

APPROVED, THESIS COMMITTEE:

Douglas Natelson, Chair
Associate Professor of Physics and Astronomy
and Electrical and Computer Engineering

Qimiao Si
Professor of Physics and Astronomy

Kevin F. Kelly
Assistant Professor of Electrical
and Computer Engineering

HOUSTON, TEXAS

November, 2007

Abstract

ELECTRON TRANSPORT IN FERROMAGNETIC NANOSTRUCTURES

by

Sungbae Lee

As the size of a physical system decreases toward the nanoscale, quantum mechanical effects such as the discretization of energy levels and the interactions of the electronic spins become readily observable. To understand what happens within submicrometer scale samples is one of the goals of modern condensed matter physics. Electron transport phenomena drew a lot of attention over the past two decades or so, not only because quantum corrections to the classical transport theory, but also they allow us to probe deeply into the microscopic nature of the system put to test. Although a significant amount of research was done in the past and thus extended our understanding in this field, most of these works were concentrated on simpler examples. Electron transport in strongly correlated systems is still a field that needs to be explored more thoroughly. In fact, experimental works that have been done so far to characterize coherence physics in correlated systems such as ferromagnetic metals are far from conclusive. One reason ferromagnetic samples draw such attention is that there exist correlations that lead to excitations (e.g. spin waves, domain wall motions) not present in normal metals, and these new environmental degrees of freedom can have profound effects on decoherence processes. In this thesis, three different types of magnetic samples were examined: a band ferromagnetism based metallic ferromagnet, permalloy, a III-V diluted ferromagnetic semiconductor with ferromagnetism from a hole-mediated exchange interaction, and magnetite nanocrystals and films.

The first observation of time-dependent universal conductance fluctuations (TD-UCF) in permalloy is presented and our observations lead to three major conclusions. First, the cooperon contribution to the conductance is suppressed in this material. This is consistent with some theoretical expectations, and implies that weak localization will be suppressed as well. Second, we see evidence that domain wall motion leads to enhanced conductance fluctuations, demonstrating experimentally that domain walls can act as coherent scatterers of electrons. Third, the temperature dependence of the fluctuations is

surprisingly strong, suggesting that the dominant decoherence mechanism in these wires is different than that in similar normal metal nanostructures.

The first observation of TD-UCF in diluted magnetic semiconductors (DMS) is also presented. In contrast to analogous measurements on permalloy samples, we find a surprising suppression of TD-UCF noise in this material at low temperatures, independent of field orientation. We believe this implies that the suppression is not due to an orbital effect, and therefore some of the fluctuations originate with time-varying magnetic disorder. The temperature dependence of the TD-UCF implies either an unusual fluctuator spectrum or a nonstandard dephasing mechanism. Measurements of UCF as a function of magnetic field allow an order of magnitude estimate of the coherence length at 2 K of approximately 50 nm in this material.

The last samples examined were magnetite nanocrystals and films. Magnetite has been used in technologies for millennia, from compasses to magnetoelectronic devices, although its electronic structure has remained controversial for seven decades, with a low temperature insulator and a high temperature "bad metal" separated by the Verwey transition at 120 K. A new electrically driven insulator-metal transition below the Verwey temperature in both magnetite films and nanocrystals was observed. The possibility that this was a thermal effect was tested through various methods, and we have shown that the transition is in fact truly electrically driven. This electrically driven transition also showed a great deal of rigidity against external magnetic field and high gate voltages.

Table of Contents

List of Figures

Chapter 1

Introduction

Over the last century, understanding the electrical transport in normal metals has been a major goal in condensed matter physics. Increasingly sophisticated models have been refined. Many experiments were performed in order to understand quantum transport phenomena as well as to check the validity of suggested theories. For roughly the last twenty years, accompanied with the development of patterning and fabrication techniques, tremendous progress has been made in this area of physics, especially for low dimensional systems. However, unlike normal metals, relatively little experimental work has been done to characterize electrical transport physics in correlated systems such as ferromagnetic (FM) metals (even when compared to the superconducting system, another example of a correlated system, the FM system is relatively unexplored).

The theoretical and experimental tools developed over the past twenty years with the normal metal systems are, indeed, very powerful tools to understand electrical transport and underlying mechanism of relevant physics. Under certain conditions, they can be applied to FM systems.

Magnetism is a subject which has been studied for nearly three thousand years. Lodestones first attracted the attention of ancient scholars, and the navigational magnetic compass was the first technological product resulting from this study. Although an early form of compass was invented in China in the eleventh century, it was not until around 1600s that anything resembling a modern account of the working of the compass was

proposed[3, 4]. Progress in the last two centuries has been more rapid, and major results have emerged which connect magnetism with other physical phenomena. An understanding of the relationship between magnetism and electricity, an inextricable link, began in 1819 by Oersted's accidental discovery. Maxwell's careful derivation of a set of four equations in 1860s led to electromagnetism. This link was further developed by Eistein's theory of relativity. And from this relativistic point of view, people started to understand more about magnetism.

However, it is the magnetism in condensed matter systems, accompanied by quantum mechanical understanding, including ferromagnets, spin glasses and low-dimensional systems, which is still of great interest today. Magnetic properties exhibited in macroscopic scale are fundamentally different from those of so called "ordinary" materials. Magnetism can be understood as a correlated phenomenon, involving the mutual cooperation of enormous numbers of particles on macroscopic length scales. Furthermore, the interest in answering fundamental questions in these systems runs in parallel with the technological drive to find new materials for use as permanent magnets, electric and magnetic sensors, or in information storing applications.

Magnetism is studied and developed with two principal aspects in mind. One is to enhance magnetic properties by finding new materials or adjusting composition of different elements within compounds that give magnetic properties. The other is to understand their electrical responses and electron transport through magnetic materials which have a long range order not existing in normal materials. Since the discovery of Hall effect in 1879 and the invention of various magnetometers (including vibrating sample magnetometer (VSM), torque magnetometer (SQUID (Superconducting QUantum Interference

Device) invented in 1964[5] is one of the most sensitive torque magnetometers), neutron scattering, Mössbauer, etc.[3]), magnetic property measurements became relatively easy to achieve. Thus, understanding of magnetic properties drastically improved. However, fully understanding transport through magnetic materials, though potentially very interesting because of the presence of an extra degree of freedom due to long range magnetic ordering, remains very challenging.

This thesis details the results of our investigations of electrical transport through FM nanostructures which include patterned metal nanowires, molecular beam epitaxy(MBE) grown dilute magnetic semiconductor (DMS) films and magnetite(Fe_3O_4) films, and chemically synthesized magnetite nanocrystals. Because of the variety of sample type and geometry, measurement techniques varied widely, from a conventional resistance measurement setup to a three terminal setup and modified bridge configuration.

Major topics which will be discussed in this thesis are divided into two categories. First one is about electrical transport through FM wire structures[6, 7]. Nanowire samples were fabricated by using 1) permalloy (Py, $Ni_{0.8}Fe_{0.2}$) via standard electron beam lithgraphy and electron beam evaporation and 2) dilute magnetic semiconductor (DMS) films via electron beam lithography and ion beam etching. After the characterization of the samples using conventional measurement techniques, the univeral conductance fluctuations were measured for detailed analysis using a modified bridge scheme. The other major topic is electrical transport through more restricted region such as nanocrystals or nanogaps formed on film samples of a strongly correlated transition metal oxide[8]. The restricted geometry may exhibit quantum confinement, and a three terminal setup is considered as an ideal tool for probing electron states of single nanoparticle in this

configuration.

This thesis is organized as follows: General ideas of ferromagnetism are further discussed in this chapter including two main models of ferromagnetism. The anisotropic magnetoresistance seen with FM materials used in our experiments is also discussed. Two other types of FM materials, dilute magnetic semiconductors and magnetite are introduced at the end. Chapter 2 describes the general idea of quantum mechanical corrections to electrical transport. This chapter is mainly focused on to understanding quantum mechanical correction of classical electron transport (mainly electrical noise including the idea of noise power). Then the description of a quantum transport phenomenon called universal conductance fluctuations (UCF) will follow. This includes a discussion of both the magnetic field-dependent UCF (MF-UCF) as well as time-dependent UCF (TD-UCF) and its external field dependence. Chapter 3 and 4 describe sample preparations, measurement methods and results of experiment for nanowire samples including both metallic nanowires and magnetic semiconductor wires, and for both nanocrystal and film magnetite samples, respectively. And chapter 5 summarizes the results and presents the outlook.

1.1 Basics

One fundamental object in magnetism is the magnetic moment, $\vec{\mu}$. "Orbital" moments arises from a microscopic current loop formed by the motion of one or more electrical charges. This is also equivalent to a magnetic dipole, so called because it behaves analogously to an electric dipole which simply consists of two opposite charges separated by a small distance. Therefore it is possible to imagine a magnetic dipole as an object which

consists of two magnetic monopoles of opposite magnetic polarity separated by a small distance. Magnetic moments can also originate from spin, the intrinsic angular momentum of a quantum particle. The electron magnetic moment is proportional to its spin via the gyromagnetic ratio g and Bohr magneton μ_B:

$$\vec{\mu} \;=\; g\mu_B\vec{S}. \tag{1.1.1}$$

Due to the nature of these objects, a full acount require quantum mechanics including quantization of angular momentum, matrix related algebra which requires operator related calculations, and state mixing when any two objects are coupled together.

1.2 Exchange Interactions

It is necessary to think about interactions between electrons because these allow the magnetic moments or spins in a solid to communicate with each other and produce the long range order that makes magnetic materials unique.

Simplest form of interaction between electrons that can be considered is the dipole-dipole interaction. Two magnetic moments μ_1 and μ_2 separated by r have an energy equal to:

$$E \;=\; \frac{\mu_0}{4\pi r^3}\left[\vec{\mu}_1\cdot\vec{\mu}_1 \;-\; \frac{3}{r^2}(\vec{\mu}_1\cdot\vec{r})(\vec{\mu}_2\cdot\vec{r})\right], \tag{1.2.1}$$

which depends on their separation and their degree of mutual alignment. It can be easily estimated that the magnitude of this effect for the case of two Bohr magnetons separated by 1 Å is approximately 10^{-23} J which is equivalent to roughly 1 K in temperature. Since many materials order magnetically at much higher temperatures (around 1000 K), the magnetic dipole interaction is too weak to be playing a dominant role in those systems.

Another effect is called exchange interaction. Exchange interactions are at their root nothing more than electrostatic interactions[9], arising because charges of the same sign cost energy when they are close together and save energy when they are apart. Exchange, however, is considered to be a main reason for a long range magnetic order. Origin of this interactions lies deeply in the idea of quantum mechanics, which can simply be described by Heisenberg model hamiltonian:

$$H \;=\; -\sum_{i\;j} J_{ij}\mathbf{S}_i \cdot \mathbf{S}_j, \tag{1.2.2}$$

where J_{ij} is the exchange constant between i-th and j-th spins.

A simple example of this would be a system with two electrons under Coloumb potential, which have spatial coordinates $\vec{r}_1$ and $\vec{r}_2$ respectively. The spatial wave function for this two-electron joint state can be written as a product of single electron states $\psi_a(\vec{r}_1)$ and $\psi_b(\vec{r}_2)$ with a consideration of the exchange symmetry. This leads to symmetric ψ_S and antisymmetric ψ_A spatial joint wavefunctions:

$$\begin{aligned} \psi_S \;&\sim\; \psi_a(\vec{r}_1)\psi_b(\vec{r}_2) \;+\; \psi_a(\vec{r}_2)\psi_b(\vec{r}_1), \\ \psi_A \;&\sim\; \psi_a(\vec{r}_1)\psi_b(\vec{r}_2) \;-\; \psi_a(\vec{r}_2)\psi_b(\vec{r}_1). \end{aligned} \tag{1.2.3}$$

For electrons the overall wavefunction must be antisymmetric so the spin part of the wavefunction must either be an antisymmetric singlet state χ_S ($S \;=\; 0$) in the case of a symmetric spatial state or a symmetric triplet state χ_T ($S \;=\; 1$) in the case of an antisymmetric spatial state. Therefore the total wavefunction can be written as either

singlet or triplet case:

$$\Psi_S \sim \psi_S \chi_S,$$
$$\Psi_T \sim \psi_A \chi_T. \tag{1.2.4}$$

And the energies of the two possible states are:

$$E_S = \int \Psi_S^* \hat{H} \Psi_S d\vec{r}_1 \, d\vec{r}_2, //E_T = \int \Psi_T^* \hat{H} \Psi_T d\vec{r}_1 \, d\vec{r}_2. \tag{1.2.5}$$

With the assumption that the spin parts of the wavefunctions are normalized, the difference between two energies is simply:

$$E_S - E_T = \int \psi_a^*(\vec{r}_1)\psi_b^*(\vec{r}_2) H \psi_a(\vec{r}_2)\psi_b(\vec{r}_1) d\vec{r}_1 d\vec{r}_1, \tag{1.2.6}$$

which is proportional to the exchange constant J. Because this is a matrix element between two states that differ solely through the exchange of the coordinates of the two electrons, the singlet-triplet energy difference is referred as an 'exchange' interaction.

Exchange interactions are divided into two categories: direct and indirect exchange. If the electrons on neighboring magnetic atoms interact via an exchange interaction without the need for an intermediary, this is known as direct exchange. Though this seems the most obvious and simple for exchange interaction to take, the reality is rarely that simple. Thus in many magnetic materials it is necessary to consider some kind of indirect exchange interaction. Another reason for the indirect exchange is because some atoms contain relatively localized d- and f-shell electrons. This allows to have large local moments but since they are localized, interactions between them often need to be mediated.

There are several different types of indirect exchange interactions known depending on the systems. For example, a number of ionic solids show magnetic ground states even

when there seems to be no direct overlap between ions that exhibit magnetic moments since those ions are usually far away from each other. The exchange mechanism that governs these type of materials is known as superexchange. In this case, magnetic moments are exchanged via non-magnetic ions such as oxygens in MnO.

In metals the exchange interaction between magnetic ions can be mediated by the conduction electrons. A localized magnetic moment spin-polarizes the conduction electrons and this polarization in turn couples to a neighboring localized magnetic moment that is away from the first magnetic moment. Again, there is no direct coupling between magnetic moments and this is called Ruderman-Kittel-Kasuya-Yosida (RKKY) interaction[3, 10].

For some other metallic oxides, it is possible to have a ferromagnetic exchange interaction which occur because the magnetic ion can show mixed valency, that is it can exist in more than one oxidation state. Some of the compounds containing Mn ions show this type of behavior when Mn ion exhibits mixed oxidation states of 3 and 4. In this type of materials double exchange mechanism is used to explain their ferromagnetic configuration (Figure 1.1). Underlying idea for this interaction is that the electron hopping from one type of oxidation state to neighboring other type of oxidation state is energetically favorable but if this neighboring state has antialigned valence electrons' spin to that of previous state valence electrons, then due to Hund's rule conduction (hopping) would not occur. Thus the system ferromagnetically orders in order to save energy.

It is also possible for the spin-orbit interactions to play a role in a similar manner to that of the oxygen atoms in superexchange. In this case, the excited state is not connected with oxygen but is produced by the spin-orbit interaction in one of the magnetic ions.

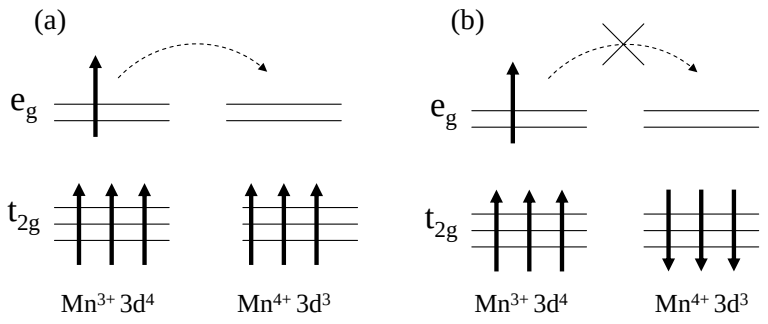

Figure 1.1: Double exchange mechanism that gives ferromagnetic ordering between Mn^{3+} and Mn^{4+} ions participating in electron transfer. The electron hopping to the neighboring ion is (a) favored if neighboring ions are ferromagnetically aligned and (b) not favored if neighboring ions are antiferromagnetically aligned.

Then an exchange interaction takes place between the excited state of one ion and the ground state of the other ion. This is known as anisotropic exchange interaction[3].

1.3 Magnetic Orders

Different types of interactions described above produce different types of magnetic ground states such as ferromagnets, antiferromagnets, ferrimagnets, helical orders, spin glasses, and nuclear ordering. A brief introduction of each type is given in this section, and some more detailed discussions of ferromagnetism will be in the following section.

A ferromagnet has a spontaneous magnetization even in the absence of an applied magnetic field, which means all the magnetic moments lie along a single direction. It is generally due to exchange interactions with positive exchange constants ($J_{ij} > 0$) to ensure ferromagnetic alignment. The origin of spontaneous magnetization was explained with Weiss model where the simple idea of mean field theory is adopted to Heisenberg

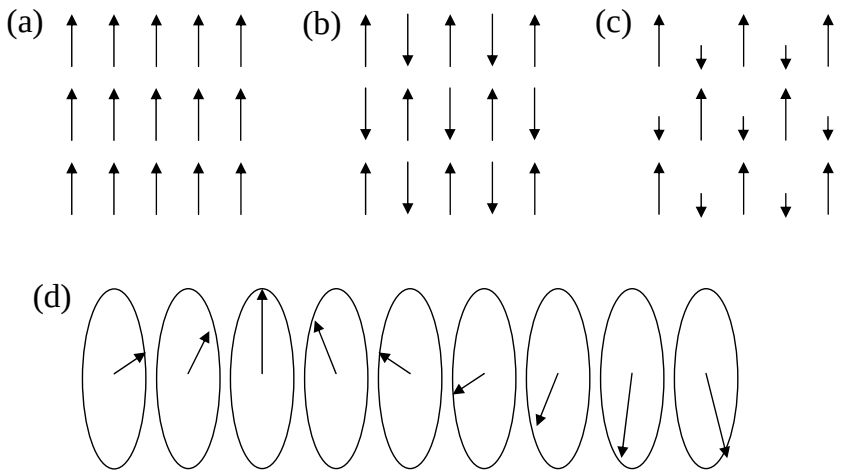

Figure 1.2: Different types of magnetic orderings are illustrated: (a) ferromagnetism, (b) antiferromagnetism, (c) ferrimagnetism, and (d) helical order.

model. The temperature scale related to ferromagnetic ordering is called the Curie temperature, T_C, above which the spontaneous magnetization vanishes; it separates the disordered paramagnetic phase at $T > T_C$ from the ordered ferromagnetic phase at $T < T_C$. In case of iron, $T_C \approx 1000$ K. In fact, it is possible to establish an approximation further by using mean field theory to link exchange constant J to the Curie temperature T_C, which gives:

$$J = \frac{3k_B T_C}{2zS(S+1)}, \tag{1.3.1}$$

with z nearest neighbors. When $S = 1$, observed Curie temperature for iron,for example, corresponds to $J = 11.9$ meV[10].

If the exchange constant J_{ij} is negative, an alignment of nearest neighbor magnetic moments becomes such that zero net magnetization becomes preferrable. This is the case of antiferromagnetism. Very often this occurs in systems which have two interpenetrating sublattices with opposite direction of magnetic moments. So if the nearest neighbors

of each magnetic moment on one sublattice come from the other sublattice, the system exhibits antiferromagnetic ordering. The transition temperature for antiferromagnetic ordering is known as Néel temperature, T_N. Typically, materials that show nonmagnetic atom mediated exchange interactions, *i.e.* superexchange interactions, exhibit antiferromagnetic ordering[10]. This is called G-type antiferromagnetism (*e.g.* MnO (T_N = 116 K), MnS (160 K), FeO (198 K)) and also found in materials such as $LaFeO_3$ and $LaCrO_3$. However, $LaMnO_3$, is known to exhibit A-type ordering. This is due to structural deformation causing alternating long and short Mn-O bonds within (100) planes. Thus, A-type ordering shows in-plane ferromagnetic and out-of-plane antiferromagnetic ordering at the same time[3].

Ferrimagnetic ordering occurs if a material shows non-equivalent magnetization from two sublattices. Simply put, magnetizations from two sublattices are in opposite directions, but their sizes are not the same. Often times, ferrimagnets are confused with ferromagnets because of the fact that their net magnetization is nonzero, so they behave somewhat similar to ferromagnets. However, because magnetization itself and its temperature dependence on each sublattice are different, the net magnetization can have quite complicated temperature dependence, and the Curie Weiss law is not applicable to ferrimagnets. One type of material showing ferrimagnetic ordering is the ferrites, and this will be discussed more in detail in Section 1.8.

Most ferrimagnets are electrically poor conductors compared to ferromagnets, which are often metallic. Thus, ferrimagnets become useful in applications when a material with a spontaneous magnetization is required to operate at high frequencies (*e.g.* transformers), since the induced voltage will not be able to cause any significant eddy currents to flow

unlike in metallic system.

In many rare earth metals, the crystal structure is such that the atoms lie in layers, and thus ferromagnetic alignment ends up within the layers. When such aligned magnetic moments within different layers interact, they can form a helical order (also know as helimagnetism) as described in Figure1.2 (d). Helical structures are found in many magnetic systems, most famously in rare earth metals. The exchange interaction in rare earth metals is an indirect RKKY interaction.

Another possible configuration with a form of magnetic order is when magnetic atoms are sparsely populated in a non-magnetic lattice with dilute and random distribution. Such system could undergoes a transition from a high temperature disordered state to low temperature "frozen disorder" state against one's intuition. Usually, in this case, the lower temperature state is not completely ordered as any of previous examples. However, it exhibits distinctly different behaviors from the high temperature disordered state. This type of ordering is called spin glass. It usually exhibits a random, yet cooperative, freezing of spins at a well defined temperature T_f (freezing temperature) below which a metastable frozen state appears without the usual magnetic long-range ordering[3].

1.4 Ferromagnetism

Even though there exist more specific categories depending on their arrangement of local magnetic moments within and their response to external magnetic field, magnetic material, when mentioned, largely referred to ferromagnetic material and magnetism to ferromagnetism in many contexts. And because electron transport in ferromagnetic nanostructure is the focus of this investigation, ferromagnetism is discussed further in

detail to give some idea how different types of ferromagnets used in our investigations are generally described based on these references: [11, 10, 12, 3, 13]. For instance, permalloy which was used to investigate electron transport in ferromagnetic nanowire contains nickel and iron. Nickel and iron both belong to the 3d transition metals whose magnetism mainly originates from the spins of the electrons in the 3d band[14]. These electrons are not localized but jump from atom to atom. This gives this type of ferromagnetism its name: itinerant electron magnetism[11].

The models for magnetic moments in a ferromagnet can be subdivided into two categories: 1) relatively isolated magnetic moments, applicable to the f-electrons in rare earth ferromagnets, 2) delocalized moments or band ferromagnetism, which describe weakly ferromagnetic materials. However, most ferromagnets are classified as intermediate situations[11], which is also the case for itinerant electron magnetism. Over the years, a substantial part of the research in magnetism has been devoted to the unification of these two limits into a general theory.

1.4.1 Isolated Magnetic Moments

Langevin assumed that a paramagnet consists of local magnetic moments or spins whose spatial directions follow a Boltzmann probability density function: $\exp(-U/k_BT)$, with the potential energy U equal to $-\mu_0\ \vec{\mu}_B \cdot \vec{H}_{EXT}$ and with $\vec{H}_{EXT}$ an external magnetic field[12]. For ferromagnets Weiss modified this concept by adding an uniform internal magnetic field H_{INT} to the external field. Weiss assumed that this field is proportional to the magnetization, $H_{INT} = w\ M_S$ with w the Weiss factor.

Brillouin modified the Langevin concept for paramagnets by taking into account that a

magnetic moment cannot rotate freely and that its expectation value is spatially quantized within an atom. The component of an electron spin along a field direction can only take on two values: parallel or anti-parallel to the local magnetic field. Therefore it can only flip. Also this theorem was modified with a Weiss-field to explain ferromagnetism as a function of temperature and external field. Although it is generally accepted that the physics involved in the local magnetic moment theories in not dominant, the Brillouin curve is in reasonable agreement with experimental results when both the saturation magnetization, M_0, and the Curie temperature, T_C are used as fitting paramenters. This also means the Weiss factor, w is a fitting parameter. And unfortunately, the resulting Weiss-field, H_{INT} is unrealistically large if explained with these classical theories.

The first physically plausible model for ferromagnetism was given by Heisenberg. In his model, H_{INT} is replaced by an exchange interaction that results from the close proximity between moments in combination with the Pauli exclusion principle[3]. There is only a short-range interaction (*i.e.* nearest neighbor interaction), but this leads to a long-range ordering. In the Heisenberg model the exchange energy between two magnetic moments i and j is equal to

$$U_{EX} \;=\; -\; 2\; J\; \vec{S}_i \cdot \vec{S}_j, \tag{1.4.1}$$

with J the exchange integral and S_i the angular momentum of the magnetic moment at ith site. Strictly speaking J depends on the distance between two moments. However, in most cases one only takes the nearest neighbors into account. Therefore, J is often treated as a constant (and zero for larger distance interactions). Heisenberg did not take spatial quantization of S into account in his model but used an electron gas configuration.

The Ising model is the one included spatial quantization.

1.4.2 Spin Waves and Magnons

A solid is considered perfectly ordered at $T = 0$, although zero-point fluctuations mean that, even then, atoms are not purely static. At non-zero temperature, the order is disturbed by thermally excited lattice vibrations, which are quantized as phonons. The behavior of phonons is then characterized by a dispersion relation. In a ferromagnetic system, non-zero temperature disturbance or magnetic order is called spin waves, quantized as magnons.

The concept of spin waves has been developed by Bloch. The classical explanation uses the Heisenberg model and combines it with the spatial freedom of the spins. At a finite temperature, if only the nearest neighbor interactions are considered, the time dependence of spin at a given site can be expressed as:

$$\frac{d\vec{S}_i}{dt} = \frac{2J}{\hbar}(\vec{S}_j \times (\vec{S}_{j-1} + \vec{S}_{j+1})), \tag{1.4.2}$$

which states that the change of angular momentum is equal to the torque that results from the interactions with the neighboring rotating spins[15]. If the spin alignment at the ground state in z-axis, then the solution for the equation 1.4.2 gives a spin wave dispersion relation:

$$\hbar\omega = 4JS(1 - \cos qa). \tag{1.4.3}$$

For small q, this can be further simplified to:

$$\hbar\omega \approx 2JSq^2a^2 \approx D_0q^2, \tag{1.4.4}$$

with a the lattice constant, D_0 the spin wave diffusion constant.

Magnons, the quantized spin waves, follow the Bose-Einstein distribution because they have a spin of one. Therefore, three dimensional density of states of magnon modes are expressed as:

$$N_{DOS} \;=\; \left(\frac{k_B T}{\hbar}\right)^{3/2} \int_0^{\infty} \frac{x^{1/2} dx}{e^x - 1} \;\propto\; T^{3/2}. \tag{1.4.5}$$

Based on this, a change in magnetization is expected to be proportional to $T^{3/2}$ for low temperature. This result is known as the Bloch $T^{3/2}$ law, and it fits very well with experimental data in the low temperature regime in case of spontaneous magnetization within a domain.

An ideal measurement for spin wave dispersions is inelastic neutron scattering because neutron scattering can probe from some μeV of quantum tunneling to several eV transitions, and typical magnon energies are in the range of $10^{-3} \;-\; 10^{-2}$ eV.

1.4.3 Band Ferromagnetism

Depending on the density of states at the Fermi level of a conduction or valence band, the band can split into a spin-up and a spin-down subband. When the populations of different spins are mismatched, there is an excess number of one type of spins and therefore a non-zero net magnetization. This is the process that takes place in Ni or Fe, and is responsible for the fact that they are ferromagnets.

The explanation will be based on Figure 1.3 at zero temperature where $M_S \;=\; M_0$. In this figure, the spin-up and spin-down bands split because of an externally applied field H, and this leads to a net magnetization, M. This process is called Pauli paramagnetism and is defined by the Pauli susceptibility, $\chi_P \;=\; \partial M/\partial H$. For small H, the number of electrons with spin-down that become spin-up is proportional to the density of states

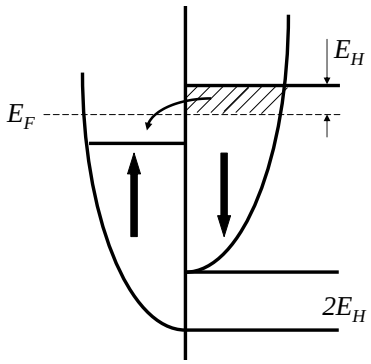

Figure 1.3: Density of states around Fermi level showing splitting of energy bands between two different spins with an external magnetic field, H.

at the Fermi Level, $g(E_F)$. Hence, $\Delta n = g(E_F)\ E_H = g(E_F)\mu_0\mu_B H$. This gives $M = 2\mu_B\Delta n$ and finally results in

$$\chi_P = 2\mu_0\mu_B^2 N(E_F). \tag{1.4.6}$$

Stoner combined this concept with the internal Weiss field to explain band ferromagnetism. Now the result becomes $M_0 = w\chi_P M_0 + O(M_0^2)$; the saturation magnetization is a function of itself. Note that there are higher-order terms introduced when a Taylor series was used for the series expansion the density of states around Fermi level. Obviously $M_0 = 0$ is a solution, however it can be shown that this is not a stable solution when

$$w\chi_P > 1. \tag{1.4.7}$$

In this case, a positive solution for M_0 is stable and therefore the material will be ferromagnetic. Equation 1.4.7 is called the Stoner condition for band ferromagnetism. This theory can successfully explain the magnitude of the saturation magnetization M_0 of various 3d ferromagnets and thteir alloys. But what this theory fails to explain is

the dependence of the magnetization upon temperature. Band ferromagnetism predicts $M_0 - M_S(T) \sim T^2$ for low temperatures[11]. But experimental results show a $T^{3/2}$ dependence[10]. Because of the band splitting into a spin-up and spin-down band, an electron will not only require a spin flip but also a certain impulse and/or energy for a transition from one band to the other. In the low temperature regime such transfers will be rare.

1.5 Domains and Effect of Surface

So far, all the ideas presented had an assumption that the magnetic moments within a given magnetic system are all aligned in a specific direction, and thus causing a specific magnetic order. However, this could not explain the fact that some exhibit stronger magnetic properties than others. This, in fact, is because magnetic materials have domain structures. Typically, magnetic materials can be divided into many small regions with uniform magnetization, called domains. And domains are separated by domain walls. Domain structure can be understood in the context of symmetry breaking. If different regions of a macroscopic system break symmetry in different ways, then in the interface between these regions the rigidity can break down. In general, domain walls, defects, vortices, dislocations and other singularities are expected to emerge around these region where symmetry breaks. In ferromagnets, the most important singularity is the domain wall.

In fact, domain structures allow magnetic samples to respond to externally applied magnetic field. This is the reason why it is possible for most of magnetic samples to attain saturation magnetization of the whole sample (corresponding to $\mu_0 M \sim 1$ T)

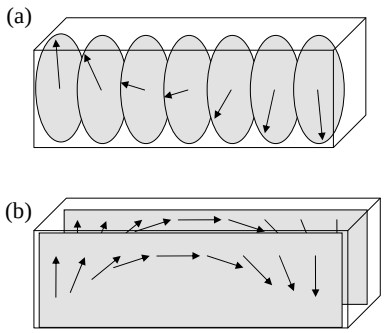

Figure 1.4: Domain walls: (a) Bloch wall and (b) Néel wall.

at a relatively weak external magnetic field (sometimes as low as 10^6 T)[3]. Such low applied fields would have negligible effect on a paramagnet. Especially large response in ferromagnetic samples is because the applied field does not have to order the magnetic moments macroscopically. Magnetic moments in the sample are already ordered, and the applied field only has to realign domains, which can be done easily by domain wall motion. Sometimes, it is observed for a ferromagnetic sample to exhibit zero magnetization under zero applied field. This is also possible by a manifestation of domains.

Beween adjacent domains there is a boundary called a domain wall. The domain walls can be classified according to the angle between the magnetization in the two domains. A 180° domain wall separates domains of opposite magnetization. And a 90° domain wall separates domains of perpendicular magnetization. There are two most common types of 180° domain walls: one is the Bloch wall, in which the magnetization rotates in a plane parallel to the plane of the wall; and the other is Néel wall, in which the magnetization rotates in a plane perpendicular to the plane of the wall (Figure 1.4). For example, from

simple calculation from Heisenberg model, Bloch wall formation costs energy:

$$\sigma_{BW} \;=\; JS^2\frac{\pi^2}{Na^2}. \tag{1.5.1}$$

Typically it costs energy to have a set of twisted magnetic moments in a system. Thus, domain walls want to unwind themselves. In order to keep domain walls as they are, it requires other interactions. A couple of such interactions are magnetocrystalline anisotropy and shape anisotropy.

Crystals possess a magnetic easy axis and hard axis. Along certain crystallographic directions it is easy to magnetize the crystal, and along others it is hard, and thus the names originate. This is an intrinsic property of the material due to the structure and exchange interactions. For example, cobalt has an easy axis along (100) direction. It requires an external magnetic field of only a fraction of Tesla (less than 0.01 T) in order to fully align magnetization moments along this direction. On the other hand, if the magnetic field is applied to (001) direction, full saturation of magnetic moment requires a lot greater field scale (over 0.1 T))[16].

The shape anisotropy is another energy term related to the orientation of the magnetization associated with the sample shape. The effect of shape anisotropy is usually greater at the surface because the magnetization prefers to align itself in the plane direction in order to save energy. In thin films, for example, shape anisotropy $\frac{1}{2}\mu_0 M^2\cos^2\theta$ (where θ is the angle between the film normal and $\vec{M}$) keeps the magnetization in the plane of film. Permalloy is another good example. A soft ferromagnet such as permalloy has weak magnetocrystalline anisotropy by design, which leaves the shape anisotropic energy a main cause of domain configuration. Thus, one can modify its domain structure

by manipulating the geometry.

Both of which leads an energetic saving for keeping the magnetization in the plane of the sample and not to propargate over the whole sample:

$$\sum_{i=1}^{N} K \sin^2 \theta_i \approx \frac{NK}{2}, \tag{1.5.2}$$

where K is anisotropy constant. Domain wall width is also determined by these energy relations. Domain wall formation elergy is proportional to $1/N$ where N is a number of sites over which spins/magnetic moments rotate, and anisotropy energy is proportional to N. Thus, the equilibrium point can be calculated. Energy stored within a domain wall is simply a sum of equation 1.5.1 and equation 1.5.2:

$$\sigma_{BW} = JS^2 \frac{\pi^2}{Na^2}. \tag{1.5.3}$$

By calculating equilbrium point for N spin involved domain wall leads to a size:

$$\delta = \pi \sqrt{\frac{2JS^2 z}{aK}}, \tag{1.5.4}$$

where z is the number of sites in a unit cell.

1.6 Magnetoresistive Effect

Magnetoresistive effect or simply magnetoresistance(MR) is the property of a material to change the value of its electrical resistance when an external magnetic field is applied to it. The magnetoresistance $\Delta\rho/\rho$ is usually defined by

$$\frac{\Delta\rho}{\rho} = \frac{R(H) - R(0)}{R(0)}. \tag{1.6.1}$$

It is technologically useful quantity as well as scientifically because magnetoresistive sensors are extensively used in many applications.

1.6.1 Negative Magnetoresistive Effect

When a metal carries a current, the displacement of electrons to different parts of the Fermi surface is such that scattering is minimized, *i.e.* the electrons find the path of least dissipation to cross the sample. Hence, if electrons are forced to take a different path, because of the presence of an applied magnetic field for example, they would take a path which leads to more scattering. Thus, in general, a *positive* MR is expected. However, in ferromagnets, a *negative* MR is observed. Nickel is a good example to explain this behavior. In nickel, only very small amount of energy is required to change the configuration from ($3d^8\ 4s^2$) to ($3d^9\ 4s^1$) or ($3d^10$). In general, Ni is considered to be ($3d^{9.4}\ 4s^{0.6}$). The d band is very narrow (which is necessary condition for ferromagnetism in transition metals so that $g(E_F)$ is large and the Stoner condition is satisfied), and hence $m_d^* \gg m_e$. And as the s bands are nearly free, $m_s^* \sim m_e$. Hence, the conductivity σ, which is given by

$$\sigma = \frac{n_s e^2 \tau_s}{m_s^*} + \frac{n_d e^2 \tau_d}{m_d^*}, \tag{1.6.2}$$

is dominated by the first term and conduction is mainly due to the s electrons. In 1.6.2, n_s and n_d are the number of electrons in the s and d bands respectively, and the scattering times are $\tau_s \sim \tau_d$.

The transition probability is mainly due to s→d transitions. At low temperatures, $T \ll T_c$, all the unoccupied d states are antiparallel, so only half of the s electrons can make transitions. For $T > T_c$, all the s electrons can make transitions, and so there is more scattering. Hence, a decrease in the resistivity below T_c is expected. If magnetic field is applied to this system, the magnetic field may increase the spin polarization and

allow fewer s→d transitions. Therefore, a negative MR is observed.

1.6.2 Anisotropic Magnetoresistive Effect

The anisotropic magnetoresistance (AMR) is a result of an anisotropy in the resistivity of the ferromagnet. Its origin is connected with the spin-orbit interaction and its influence on s-d scattering[3]. The resistivity parallel to the magnetization, $\rho_{\parallel M}$, can differ from the resistivity perpendicular to the magnetization, $\rho_{\perp M}$, because the scattering probabilities for conduction electrons depend on the magnetization angle.

Suppose that the magnetization makes an angle ϕ with current density J_{DC}, which is used to measure the resistivity. Figure 1.5 illustrates this idea. Because the resistivity consists of two parts, $\rho_{\parallel M}$ and $\rho_{\perp M}$, the electric fields in these directions will differ: $E_{\parallel M} = \rho_{\parallel M} J_{DC} \cos\phi$ and $E_{\perp M} = \rho_{\perp M} J_{DC} \sin\phi$. As a result, the electric field parallel to J_{DC} becomes $E = E_{\parallel M} \cos\phi + E_{\perp M} \sin\phi$. This leads to the measured resistivity, $\rho = E/J_{DC}$. If the magnetization is uniform throughout the sample, the resistance between the contacts becomes

$$R(\phi) = R_0 + R_\Delta \cos^2\phi, \tag{1.6.3}$$

with ϕ an angle between the magnetization and the applied current, $R_0 = R_{\perp M}$ which is calculated from $\rho_{\perp M}$ and $R_\Delta - R_{\perp M}$. At room temperature thin film (40 nm) permalloy gives $R_\Delta/R_0 \approx 2\%$[14, 17].

1.7 Diluted Magnetic Semiconductors

One of the materials explored in this thesis was $In_{1-x}Mn_xAs$ which is categorized as a III-V diluted magnetic semiconductor (DMS). Diluted magnetic semiconductors based

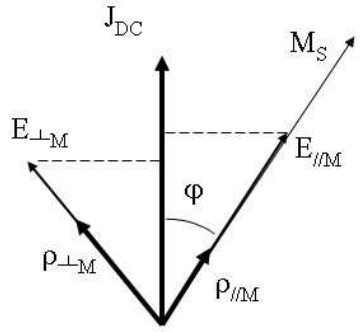

Figure 1.5: This illustrates an anisotropy in resistivity of a ferromagnet which leads to the AMR effect. The applied current density J_{DC} is in an agle ϕ with the magnetization M_S.

on III-V compounds are relatively new class of materials compared to the ones based on II-VI compounds. One of the reasons was because, unlike the II-VI compounds, III-V compounds have been found difficult to dope with Mn: for example, bulk crystals of (Ga, Mn)As typically have Mn content only up to a few tenths of a percent. It was only recently become possible with an advent of off-equilibrium crystal growth by molecular beam epitaxy (MBE), to make high Mn content samples such as $In_{1-x}Mn_xAs$ and $Ga_{1-x}Mn_xAs$[18].

Typically, Mn atoms introduced in GaAs or InAs tend to segragate to form MnAs because the stable crystal structure of MnAs is different from zincblend structure of GaAs and InAs. Thus, Mn solubility is severely limited in the equilibrium condition, and it requires to maintain off-equilibrium condition during the MBE growth in order to make InAs or GaAs structure to accept higher percentage of Mn atoms without segregation[19].

Depending on Mn concentration and substrate temperature[20] used during the growth process, carrier density varies widely and even the carrier type (p or n) changes. It is

p-type that is typically preferred because it is known that the most interesting feature of all, ferromagnetism, in this material is strongly tied to the presence of mobile carriers (holes) that dominate conduction. Two features of the holes are important: one is the delocalization of holes from the impurity, and the other one is the interaction between the hole and the magnetic impurity (p-d interaction). In fact, the co-existence of both effects allows to mediate long-range exchange interaction between Mn atoms[21]. This long-range interaction, although still debated, can be understood in two ways. One is the RKKY exchange interaction where delocalized hole plays the role of mediating magnetic moments instead of conduction electrons[22]. In comparison to metallic systems with dilute magnetic impurities, the Fermi wavenumber in DMS is much smaller so that the ferromagnetic range is expected to be much longer than the usual metallic case. Another line of thought emphasizes the d-character of the holes and attribute the ferromagnetic interaction to a kind of double exchange mechanism based on a strong Hund coupling at the Mn site[23].

The major interest in DMS materials lies in the possibility towards practical use where transport and magnetism are intimately correlated such as the spin-transport in semiconducting devices. DMS is considered one of promising materials that make possible the injection of spin-polarized eletrons into a semiconductor at room temperature. Other applications include opto-electronics. Since GaAs and other III-V compounds are the key materials for the mordern opto-electronics, one may expect the III-V compound diluted magnetic semiconductors to open the future of opto-magneto-electronics. One of current major objectives with these materials is, therefore, to have a better understanding of

physical mechanisms governing the exchange interactions so to allow us to fine-tune magnetic properties such as Curie temperature, magnetoresistive effect, and optical responses of the materials[18, 21].

1.8 Magnetite

Magnetite (Fe_3O_4) was another magnetic material used in our research. Unlike other materials, magnetite is categorized as a ferrimagnet, one of transition metal oxides and a member of the spinel group. It has the Curie temperature of around 860 K and is known as the most magnetic of all naturally occuring minerals on Earth. In fact, this is the one that is known as loadestone, and used as an early form of magnetic compass. Just like in many other transition metal oxides, magnetite is expressed by a special chemical formula $MO{\cdot}Fe_2O_3$ where M is Fe in case of magnetite and form a special crystal structure, called reverse spinel structure[3]. This contains two types of lattice sites, tetrahedral sites (with four oxygen neighbors, these are known as A sites) and octahedral sites (with six oxygen neighbors, these are known as B sites). There are twice many B sites as A sites. The two sublattices are non-equivalent because there are two types of crystallographics site and they contain two types of different ion. In inverse spinels the Fe^{2+} cations sit at half of the B sites, while the Fe^{3+} cations occupy the other half of the B sites and all the A sites. In inverse spinels, the moments of the Fe^{3+} cations on the A and the B sites are antiparallel, so that the total moment of the sample is due to the Fe^{2+} ions only. A double exchange interaction ferromagnetically aligns the Fe^{2+} and Fe^{3+} ions on the B sites and the Fe^{3+} inos on the A sites are coupled to the Fe^{3+} ions on the B sites by an antiferromagnetic superexchange interaction. Thus, the two sets of Fe^{3+} ions cancel out,

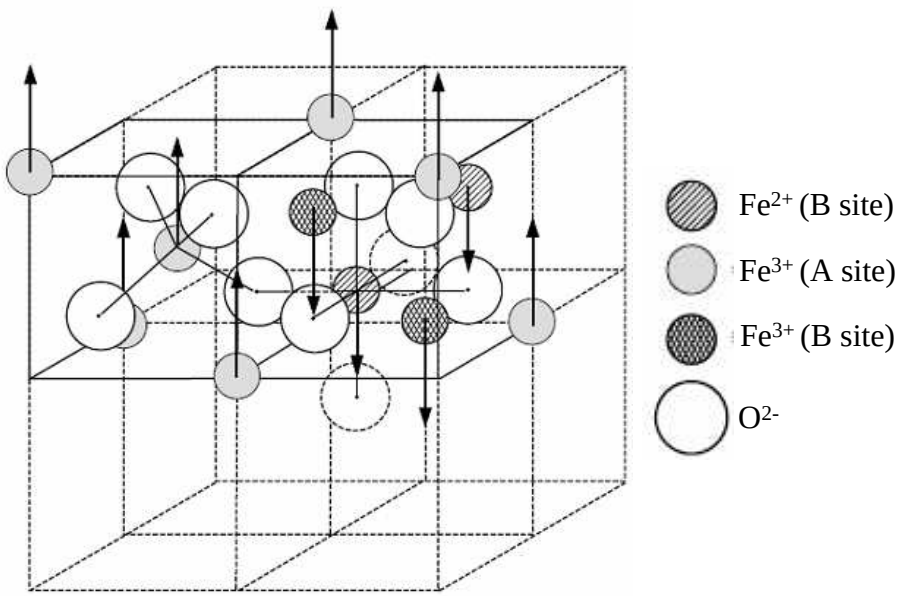

Figure 1.6: Lattice model of the inverse spinel magnetite[1]. Arrows on every iron sites indicate their magnetization orientations.

leaving a net moment due to the Fe^{2+} ions alone. The measured magnetic moment per formula unit is very close to the expected 4 μ_B due to just the Fe^{2+} ions[3, 13, 1].

Magnetite is interesting not only because it exhibits complex structural configurations or strong magnetic correlations, but also because it exhibits charge ordering and sharp electric and lattice symmetry transition around 122 K, known as Verwey transition. At higher temperature, magnetite is considered semiconductor or bad metal. However, below the transition temperature, it is observed that the bulk resistivity of magnetite sharply jumps, and material starts to exhibit insulating behaviors. Verwey transition was first discovered by E. J. W. Verwey in 1939 with magnetite[24]. Verwey's original model lies on the fact that this material has an inverse spinel structure. This, first of all, explains rather low bulk resistivity ($10^{-5} < \rho < 10^{-3}$ Ω m) of magnetite above transition compared

to other normal spinel structure transition metal oxides (typically ranges around 10^5 Ω m)[1]. Verwey proposed that the Fe^{2+} and Fe^{3+} ions, above critical temperature (Verwey temperature, T_V), to be randomly distributed over the B sites, permitting relatively easy valency exchange according to the Equation 1.8.1 by means of thermally activated fast electron hopping.

$$Fe^{2+} \; - \; e^{-} \; \leftrightarrow \; Fe^{3+}. \tag{1.8.1}$$

Upon cooling below T_V, together with the reduction of the crystal symmetry from cubic to tetragonal (later reinterpreted as orthorhombic), charge ordering was proposed in a way that successive lattice planes would be occupied, alternatively, by two- and three-fold Fe ions.

Unfortunately, it is still uncertain what exactly triggers Verwey type transition although there are many different experimental results available such as resistivity[24], specific heat[25], sructural deformation[26], Magnetic After-Effect[27], etc., that are considered to be closely tied to Verwey transition. It is not even certain whether which one(s) is/are major reason(s) for this transition.

Chapter 2

Universal Conductance Fluctuations

Mesoscopic physics deals with the physics of small condensed matter objects. This is a popular research discipline even though a clear-cut definition is not straightforward[28]. Mesoscopic and macroscopic systems have in common that they both contain large number of atoms. A first difference is that the macroscopic system can be well described by the averaging properties of the material from which it is made. This assumes that the length scales related to the system are small compared to the feature size of the device, so that the most of effects can be understood as an averaging effect by many kinds of relaxation processes. The mesoscopic system, in contrast, is so small compared to the macroscopic system that fluctuations around the average become important. A second difference is that the macroscopic system obeys (to a good approximation) the laws of classical mechanics, whereas the mesoscopic system is so small that these laws must ne corrected to account for quantum effects. Mesoscopic and microscopic systems both belong to the quantum mechanics regime.

2.1 Quantum Coherence

Understanding the properties of an electron on the microscopic scale requires quantum mechanics. However, a semiclassical model, *e.g.* Drude model, which can be represented by its conductivity expression of $\sigma = \frac{ne^2\tau}{m}$[9], is also very effective at describing the properties of electrons in macroscopic system at room temperature. In this macroscopic

regime, quantum corrections to semiclassical conduction are usually negligible due to decoherence, the suppression caused by inelastic scatterings of the electrons of quantum mechanical contributions to electron probability distributions. On the other hand, when the system size shrinks to the submicron level and the temperature of the system becomes substantially lowered, the coherence of the electron wavefunctions becomes increasingly prominent, and quantum mechanical correction starts governing the corrections of electron transport. This is simply because electrons are not classical, non-interacting entities. These corrections are known as quantum transport phenomena.

Consider adding a single electron to a system. The wavefunction of this electron will have a well-defined phase, ϕ which will be accumulated via the Hamiltonian as long as this electron is scattered elastically (usually, elastic scattering sources are static disorders such as grain boundaries and crystal defects). However, when an electron undergoes inelastic interactions with dynamic scatterers (*e.g.* another electrons, phonons, and magnetic impurities), its phase is relaxed due to entanglement with those degrees of freedom. Hence, the coherence time, τ_ϕ (or coherence length, L_ϕ) can be defined as the characteristic time (or length) over which the phase of an electron becomes uncorrelated with its original phase. In a diffusive system (system size, L being larger than the electron's mean free path, l) with electron diffusion constant, D, the relation between the coherence length and coherence time is given as $L_\phi = \sqrt{D\ \tau_\phi}$.

Decoherence depends strongly on sample temperature because many of the inelastic processes are driven by thermal energy. A typical coherence length in a thin metal film at room temperature is 1 - 2 nm, while it is close to 1 μm at 1K. At such low temperatures, electron-electron scattering becomes a dominant decoherence process because

effects due to phonons freeze out fairly quickly as temperature goes down. Perturbative calculations[29] predict $\tau_\phi \rightarrow \infty$ as $T \rightarrow 0$, with a particular power law for the divergence that depends on dimensionality (determined by comparing L_ϕ with L, w, and t, characteristic sample length, width, and thickness, respectively).

Quantum coherence must be inferred from its effects on electronic properties. There are several quantum interference corrections to the conductance that may be used to infer L_ϕ. Aharonov-Bohm (AB) oscillations, weak localization (WL), and time-dependent (or external magnetic field-dependent) universal conductance fluctuations (UCF) are well-known.

Although the work presented in this thesis is only closely related to universal conductance fluctuation theory, it is worth exploring the Aharonov-Bohm(AB) effect since understanding this gives a great deal of insight into the theory explaining the phenomena of interest.

Before trying to understand specific cases, it is useful to discuss quantum coherence briefly. Quantum interference raised by the fact that 1) electron has wave properties, 2) there are multiple possible paths electron can take, and 3) its probability leads to cross terms that can be thought of as interference terms since only these cross terms will depend on the relative phase of each electron path. This is identical to the interference seen in optical phenomena.

However, there are limitations of such interference. Just as in the optical case, in order for interference to occur, interacting waves must be phase coherent. In the case of quantum interference of electron, the interference is a result of a single electron taking different paths. Thus, initial phase coherence should be present between each path. So it

comes down to how far a electron can travel with maintaining the initial phase coherence because if electron's phase looses its initial coherence after traveling far enough or after inelastic scattering, its wavefunction would not interfere with other wavefunction.

There are usually three different scattering processes that cause dephasing of conduction electrons: electron-electron interactions, electron-phonon interactions, and spin-flip interactions. The e-e and e-ph interactions have a strong temperature dependence while spin-flip interaction is more strongly dependent on the non-zero magnetic moment impurity concentration.

The total inelatic scattering length of electron, which is equal to electron coherence length can be calculated using Matthiessen's rule resulting in:

$$L_{tot}^{-2} \;=\; L_{e-e}^{-2} \;+\; L_{e-ph}^{-2} \;+\; L_{sf}^{-2}, \tag{2.1.1}$$

In addition to three given causes, spin-orbit scattering can alter the coherence length. When this occurs L_{tot} and coherence length, L_ϕ are not equivalent and equation 2.1.1 must be altered.

It is not surprising that the coherence length also sets the dimensionality of given sample when discussing quantum transport phenomena. If a system has sides larger than the coherence length in all three dimension, the system is considered three dimensional and so on. System dimensionality is very important because most of behaviors related to quantum transport phenomena have strong dimensionality dependence.

2.2 Aharonov-Bohm Effect

As mentioned earlier, AB effect is a good example to understand quantum interference because it has by far the simplest configuration. In a higher dimensional system, an

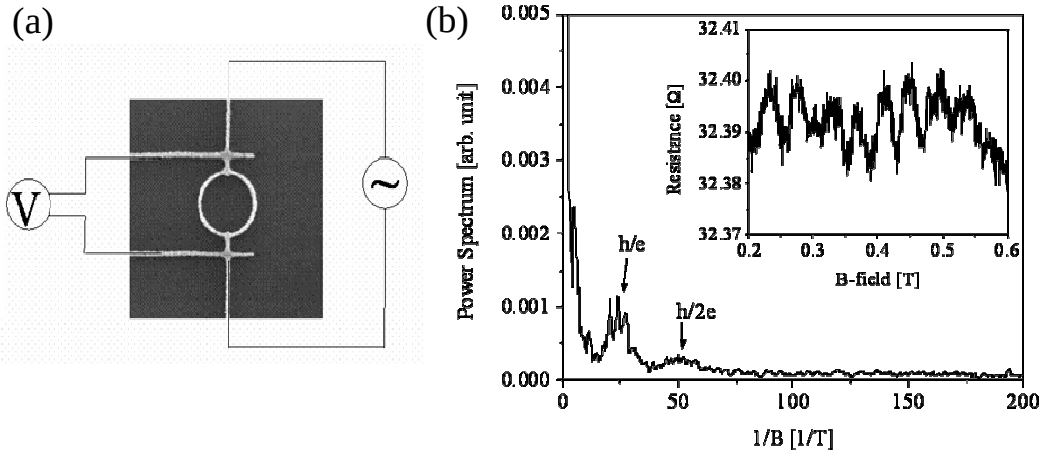

Figure 2.1: (a) Schematic diagram for the measurement with SEM image of silver AB ring whose diameter is 380 nm. (b) Power spectrum of resistance as a function of inverse B-field at 1.7 K. Inset shows the raw resistance versus B-field data whose oscillation period ($\sim$ 37 - 40 Oe) is clearly shown.

electron can have many possible paths to take whereas in a lower dimensional system possible paths are limited. Which means that if a system size is reduced further down so that only one side is longer than the coherence length, an electron path can be limited to one, *i.e.* electron path can be physically controlled. AB effect is based on this idea. By designing a sample as in Figure 2.1 (a), passible electron paths are limited to two.

When there are only two available paths, probability of an electron to be at any point $\vec{x}$ becomes simply:

$$P(\vec{x}) \;=\; |A_1|^2 \;+\; |A_2|^2 \;+\; 2|A_1^* A_2| \cos(\phi_1 \;-\; \phi_2), \tag{2.2.1}$$

where, sub-indices 1 and 2 indicate two different paths. The conductivity should therefore oscillate with a changing phase difference between two paths. One of the simple means to change phase is to apply varying external magnetic field. This results varying magnetic

vector potential which changes phase of electron's wavefunction as

$$\phi \;=\; \phi_0 \;+\; \int (\vec{k} \;+\; \frac{e}{\hbar}\vec{A}) \cdot d\vec{l}. \tag{2.2.2}$$

where $\vec{l}$ is the electron path and $\vec{A}$ is the magnetic vector potential. Thus, the phase differnece is found to be:

$$\phi_1 \;-\; \phi_2 \;=\; \frac{eAB}{\hbar}, \tag{2.2.3}$$

where A is the area of the ring and B is the applied field strength.

Now, by plugging equation 2.2.3 into equation 2.2.1 gives oscillating term with respect to the magnetic flux with a period of h/e. An example of this is given in Figure 2.1 (b). And the minimum possible coherence length at the given temperature can simply be a half of the circumference of the ring shape path.

AB effect in FM materials were also studied[30, 31], and in case of NiFe nanoring devices, the coherence length was measured to be around 500 nm at $T \;=$ 50 mK[30]. Compared with the coherence length in typical normal metals around 30 mK, such as Au ($\sim$ 2 μm) and AuPd ($\sim$ 1.2 μm), this is considerably small. Which makes this type of measurement more challenging for FM materials since either the temperature should be substantially lowered in order to see any significant oscillation features or the patterned samples should have extremely small size.

The last thing needed to emphasize is the fact that an electron's phase can be altered by a varying magnetic field applied perpendicularly. This is one of main idea keep occuring in other quantum phenomena including UCF.

2.3 Universal Conductance Fluctuation Theory

2.3.1 Thermal Noise

In the system of interest, two types of noise sources are important. One is Johnson or thermal noise, and the other one is excess or $1/f$ noise. Thermal noise, also called Johnson noise, is basically due to thermally excited random motion of electrons in metals whereas $1/f$ noise is due not to electron motion but to defect motion. There are two distinct characteristics in excess noise. The first is that it has an inverse-frequency $(1/f)$ dependence. The second is its complicated temperature dependence.

Thermal noise can be attributed to the thermally agitated random motion of the electrons in a metal. Theoretical derivation using classical statistics, themodynamics, and basic idea of electronics gives total noise power expressed as:

$$P(f)\Delta f \;=\; k_B T \Delta f, \tag{2.3.1}$$

where Δf represents bandwidth. Or equation 2.3.1 can be modified to:

$$V^2 \Delta f \;=\; 4 k_B T R \Delta f, \tag{2.3.2}$$

Equation 2.3.2 has no frequency dependence so the time average of V^2 should be:

$$< V^2 >_t \;=\; 4 k_B T R \Delta f, \tag{2.3.3}$$

As stated, thermal noise has no frequency dependence. And it depends linearly on temperature. Thus, the effect due to the thermal noise at the temperature scale in which we are interested should be quite small. For example, 100 nm wide Py nanowire sample (Sample C from Table 3.1) gives voltage fluctuations of approximately 5×10^{-19} V^2/Hz, which, if properly normalized, gives $\sim 5 \times 10^{-22}$ Hz^{-1}. This number is almost 10 orders

of magnitude smaller than the $1/f$ noise power obtained at a given temperature from our experiment.

2.3.2 Excess Noise

As mentioned, the excess noise comes from defects or impurity motion rather than electron motion and shows inverse frequency dependence and complex temperature dependence. Both of which can be explained with classical statistics at high temperature, but as temperature goes down, the classical model fails to explain upturn in the $1/f$ noise power.

Suppose one defect has two possible locations in a sample resulting in two different resistance values. Simply put, suppose an impurity has two distinct scattering cross sections. It may be modeled as a two level system (TLS). If the resistance versus time of such a system is measured, a series of random steps between the two resistances will be observed. This is known as a random telegraph signal. It is shown in ref. [32] that the noise power spectrum of this random telegraph noise[33] is

$$S_R(f) \sim \frac{\tau}{1+(2\pi f\tau)^2}. \tag{2.3.4}$$

In this case, the characteristic time τ is defined as:

$$\frac{1}{\tau} = \frac{1}{\tau_1} + \frac{1}{\tau_2}. \tag{2.3.5}$$

where τ_1 and τ_2 are the characteristic times the defect stays in each state.

In the system of interest, there should exist a large number of TLS, with a broad range of characteristic times[34]. Hence, the resultant noise power is accomplished by

integrating equation 2.3.4 over τ:

$$S(f) \sim \int \frac{D(\tau)\tau}{1+(2\pi f\tau)^2} d\tau, \tag{2.3.6}$$

with distribution function $D(\tau)$of the characteristic times. If $D(\tau)$ is proportional to $1/\tau$, then the power spectrum will be $1/f$. It is shown that this is, in fact, the case for both high and low temperature[32, 34, 35] limits. This $1/f$ noise caused by the motion of scattering sites is known as local interference noise.

Another important part of excess noise is its amplitude. Since the number of mobile impurities and their motion cause $1/f$ noise, it should become smaller as temperature decreased. This is indeed true at high temperature[36]. However, at lower temperature, $1/f$ noise is observed to increase as the temperature is lowered[36, 37]. The theory as it stands is not capable of explaining this behavior. The fact that the noise increases as the temperature is lowered makes quantum interference a prime candidate to explain the phenomenon.

2.3.3 Magnetofingerprint

Conductance in a mesoscale system is the result of the interference of all possible electronic trajectories through the sample. The AB phase, for example, deterministically alters the relative phases of these complicated paths, leading to sample-specific, reproducible conductance fluctuations which are not directly dependent on the orientation of scattering sites within a coherent volume.

Magnetic field dependent universal conductance fluctuations (MF-UCF), also called magnetofingerprint (MFP), strongly depends on the location of each scattering site. Thus, the interference pattern produced by interesting paths should also be specific to the

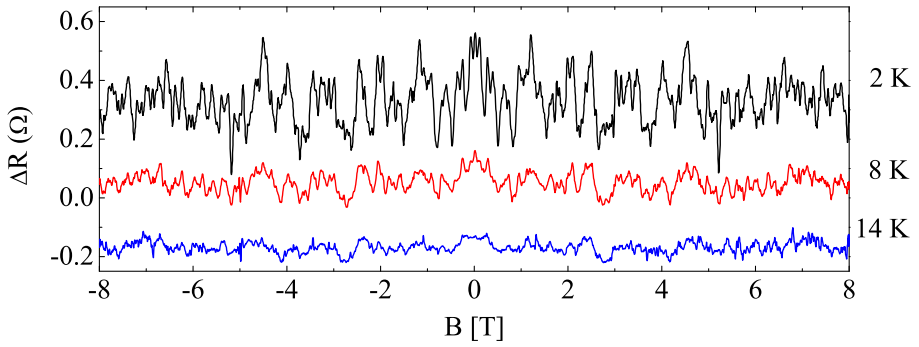

Figure 2.2: The magnetofingerprint of a 125 nm wide Ag wire sample with perpendicular magnetic field. Curves are offseted for clarity. It clearly shows the temperature dependence of the feature[2].

location of each defect. The idea behind this starts from the hypothesis that any effect resulting in a change to the interference pattern of an electron wavefunction is equivalent to change in the impurity configuration of the system[38].

As in AB effect, a specific perpendicular magnetic field produces a phase change in each electron path. This means that every field strength corresponds to a specific interference pattern that is reproducible each time that field is applied to the system. However, each system has a unique arrangement of scattering sites so the resultant interference pattern is sample-specific. Therefore a reproducible, sample-specific conductivity fluctuation should be observed in a diffusive metallic system as an applied perpendicular magnetic field is swept. Thus, comes the name magnetofingerprint. An example of a MFP at different temperatures is given in Figure 2.2.

The typical correlation field is set by the flux through a typical coherent loop which could have various size within coherence length (thus various correlation field). Within a coherent volume and ignoring thermal smearing, the typical conductance fluctuations

can be calculated independent of the details of the sample from the conductance variance which gives:

$$\delta G^2 \;=\; \left\langle (G - \langle G \rangle^2 \right\rangle \;\approx\; \left\langle \left(+ - \frac{e^2}{h} \right)^2 \right\rangle \;=\; e^4/h^2. \tag{2.3.7}$$

One last important detail to mention is the ensemble averaging effect. This is why the size of the magnetofingerprint gets smaller at higher temperature. Above idea does not include the fact that as temperature increases, coherence length L_ϕ gets shorter, and when the system size becomes longer than L_ϕ (which is always the case for our samples), averaging effect must be taken into account.

To calculate the expected size of the MFP, simply treat each coherent volume as an independent fluctuator. Thus, it can be shown:

$$\left(\frac{\delta G}{G} \right)^2 \;=\; \frac{1}{N} \left(\frac{\delta G_\phi}{G_\phi} \right)^2, \tag{2.3.8}$$

where G_ϕ is the conductance of one coherent volume and N is the number of coherent volumes in the sample.

There is also energy averaging effect we can consider. Energy averaging arises due the available energy states of conduction electrons. Such energy states can be defined by Thouless energy, $E_c \;\equiv\; \hbar D/L_\phi^2$ [39] which is also known as the coherence energy. The Thouless energy defines a "width" in the conduction band, which contains available states electrons can access. When $k_B T \;>\; E_c$, the electrons can access more than one Thouless width worth of available states. Each Thouless width is uncorrelated with the others resulting in a thermal averaging that is dependent on the number of Thouless widths.

2.3.4 Time-Dependent Universal Conductance Fluctuations

In the MF-UCF, the conductance fluctuations are due to vartying magnetic field changing electron's phase thus changing the resultant interference pattern just as in case of AB effect. This, in fact, can be considered as a field-driven 'simulated' mobile TLS. However, even at very low temperature, there should be actual mobile TLS in a metal. And these actual mobile TLS should affect the conductance in a similar manner to the 'simulated' mobile TLS. However, observation method should be time-dependent ($\delta G(t)$) rather than field-dependent ($\delta G(B)$).

The conductance change for a single mobile TLS can be written using diagrammatic methods and it gives as [40, 41]:

$$\delta G_1^2 \approx \left(\frac{e^2}{h}\right)^2 \left(\frac{\Omega}{N l_e^d}\right) \left(\frac{L}{l_e}\right)^{2-d} \alpha(k_f \delta r), \tag{2.3.9}$$

where $\alpha(k_f \delta r) = 1 - \left(\frac{\sin(x/2)}{x/2}\right)^2$, Ω is the sample volume and d is the sample dimensionality. And since, there are more than one impurity in a typical system, the net effect of multiple TLS is additive. Hence, depending on the system size, the total conductance variance within a coherent volume should be:

$$\delta G_\phi^2 = \delta G_1^2 \, n_s(T) \Omega_\phi, \tag{2.3.10}$$

where n_s is the concentration of TLS with changing scattering cross sections, and coherent volume Ω_ϕ defined as $L_x L_y L_\phi$, $L_x L_\phi^2$, or L_ϕ^3 depending on the dimensionality of the sample being 1D, 2D or 3D, respectively. It is important to note that equation 2.3.10 has an upper limit of e^2/h.

Just as in the MFP case, averaging effect should be considered for many TLS system. And the sample size should also be considered. Since typical sample size is usually larger

than a coherent volume, it is quite reasonable to start from considering $G = G_\phi/N$ and N being a number of coherent volume in a given system. After considering all the suitable substitutions, the expected conductance change due to quantum interference, in 1D system for example, is:

$$\delta G_{1D}^2 \approx \left(\frac{e^2}{h}\right)^2 n_s(T)(k_f l_e)^{-2} \left(\frac{l_e L_{th}^2 L_\phi^3}{L_z}\right)^3 \alpha(k_f \delta r), \tag{2.3.11}$$

and from equation2.3.6, the expected noise power should be:

$$S_V \approx I^2 R^4 \delta G^2 \int \frac{D(\tau)\tau}{(\omega\tau)^2 + 1} d\tau. \tag{2.3.12}$$

Note that the noise power is written in voltage noise power form. That is because the noise measured in the experiments was voltage noise, not conductance noise though the relation between two is quite simple:

$$\left(\frac{\delta G}{G}\right)^2 = \left(\frac{\delta R}{R}\right)^2 = \left(\frac{\delta I}{I}\right)^2 = \left(\frac{\delta V}{V}\right)^2. \tag{2.3.13}$$

In normal metal case, expected temperature dependence of $n_s(T)$ is T and L_{th}^2 is T^{-1}. Therefore the only temperature dependence is due to L_ϕ and R. Another important point that need to be mentioned in case of normal metal system is the fact that the overall noise power can be broken into two equally contributing parts at zero field called cooperon and diffuson contributions[42]. The cooperon is the set of all paths in a disordered system that contain time-reversal symmetry whereas diffuson is the paths without this symmetry. Therefore if sufficient magnetic field is applied to the system, cooperon contribution can be completely suppressed, and the total noise power drops by a factor of two. And the field scale over which this occurs should be dependent on the coherence length of the

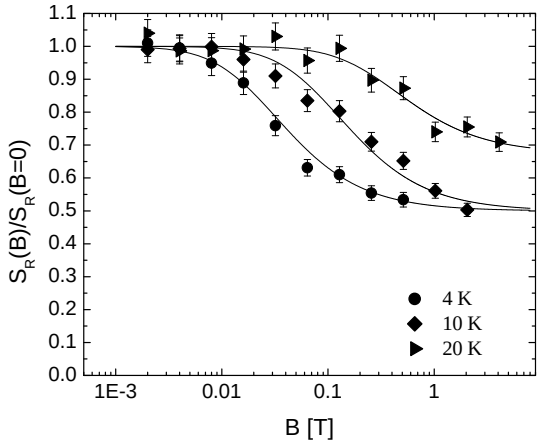

Figure 2.3: Normalized noise power vs. applied magnetic field at various temperatures for a 500 nm-wide AuPd nanowire.

system. Thus allows us to calculate the related coherence length of the system at a given temperature[43, 44].

2.3.5 Example: AuPd Wire

TD-UCF noise data are presented in the form of normalized noise power at various fields at given temperature. Figure 2.3 shows what typical normal metal sample's TD-UCF noise behaves under various external magnetic field at different temperatures[2]. Note that the noise power drops by a factor of two at a finite field due to suppression of cooperon contributions. From this data set, a coherence length can be inferred for each temperature by using a fitting function. Unfortunately, there is no analytic form for fitting function so it has to be done numerically. The numerical form is explained in detail in ref. [35, 2]. Solid lines in Figure 2.3 are the ones calculated from fitting process.

2.4 Quantum Coherence in Ferromagnetic Systems

Quantum corrections to conduction in FM systems are of fundamental interest due to correlation-induced degrees of freedom not present in normal metals (*e.g.* domain wall motions, spin waves), and these new environmental degrees of freedom can have profound effects on decoherence processes although the measurement and understanding the phenomena become more challenging because of the same reason.

It is sometimes advantageous to use transport measurement to understand magnetic properties of material. It may sound indirect and overly complicated. But in case of a domain wall motion, it is already shown[45, 46] that this, in fact, is true. The change of the magnetization associated with a depinning of a domain wall by the dissipation of the conduction electron is very small and thus, very difficult to observe directly *e.g.* by SQUID. The transport measurement, on the other hand, allows us to detect a very small change of magnetic properties as a change of resistance quite easily. It is estimated that a motion of wall over a distance of 10 nm or less can raise large as 0.2 % ($\delta\rho \approx 2 \times 10^{-9}\Omega$ cm) change in resistivity which can be easily measured. This clearly shows that the conductance of mesoscopic ferromagnets is expected to be highly sensitive to domain wall motions[46], just as the conductance of a normal metal is sensitive to the motion of an individual scatterer[40]. If domain walls coherently scatter electrons, then their motion can lead to UCF[38]. Also, if domain walls can inelastically scatter electrons, the domain wall motion can lead to electron decoherence.

Spin wave, also known as magnon when quantized, a collective modes of demagnetization in a exchange-coupled spin system, is also one of the long range orderings present

in magnetic materials, which raises the change in conductance. The relation between these and electron conductance can be very interesting since spin waves are related to spatially long range of ordering of spins, and the adjacent spins maintain a great degree of alignment (strongly corelated). They are for the spin system what phonons are to a crystal lattice[13]. Thus, electron-magnon scattering is another possible decoherence mechanism in FM metals that is not present in normal metals.

Recently, a few theoretical[47, 31, 48] and experimental[45, 49, 50, 51] reports studied mesoscopic transport properties related to these collective modes. Although very short phase coherence lengths were reported from handful experiments[50, 51], general understanding of phase coherence, especially of electron coherence length, in FM materials is still largely unexplored.

Other than lack of well established theories to explain experimental results, there are still a couple of problems to keep in mind. In FM systems, the AMR complicates the measureements of WL and MF-UCF, the two most popular methods of inferring L_ϕ, because those two measurements rely on magnetoresistive measurements. Hence, in our experiments, the TD-UCF measurement was considered mostly. Another down side of using TD-UCF measurements for FM systems is that, unlike normal metals, cooperon contributions in FM systems are rather more complicated due to internal magnetization. Depending on the given system, cooperon contributions could be included for selected types only[46] or even entirely excluded[6] which compicates the calculations for the coherence length from noise power data. Nonetheless, TD-UCF measurement provides useful insights on several aspects whcih will be discussed further more in later chapters.

Chapter 3

Nanowires

3.1 Fabrications

3.1.1 Permalloy

Samples consist of the wire at the center and five or more leads on top of the wire, equally spaced by 10 μm from the nearest ones. Both of which were patterned using standard electron beam lithography.

Sample fabrication started by cleaving 5 mm by 5 mm chips of undoped GaAs. In order to achieve continuous wire and smooth film surface specs of dust and/or remaining residue should be thoroughly removed. To this end, chip was cleaned first using lintless swabs soaked in acetone. Then it was placed under a UV lamp for 5 to 10 minutes. Once cleaned, 495 PMMA e-beam resist was spin-coated at 3000 rpm for 40 seconds. The chip was then baked on a hot plate for an hour at 165 °C to evaporate away the solvent in the resist.

The wire part was made first by drawing a single path line using scanning electron microsope. When pattern was drawn dosage was controlled to have various widths from 27 nm to several hundreds of nm. Just before the deposition, the sample was developed using 3:1 mixture of 4-methyl-2-pentanone (MIBK) and isopropanol (IPA) and once again put under a UV lamp for another 5 minutes. The in-lab Edwards FL 400 evaporator was used for all deposition except Pt deposition for the nano junction devices. 10nm of Py was deposited at a rate of 0.1 nm/sec. Liftoff was done simply by putting the sample in

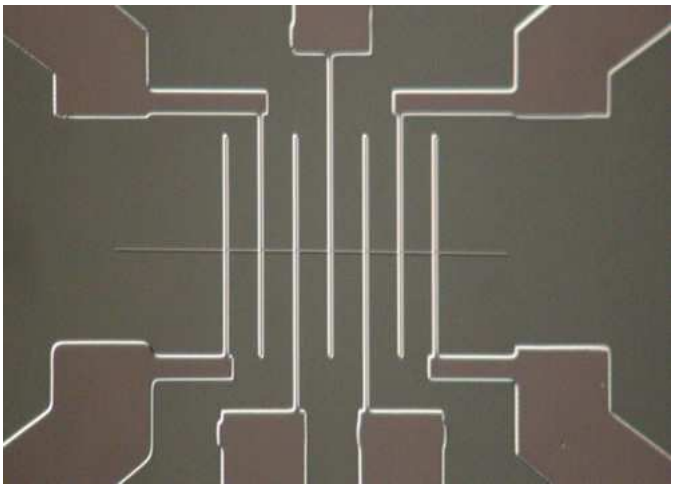

Figure 3.1: The lead-wire pattern used to fabricate all the measured samples. The leads start from large contact pads and taper down to the leads in the image. Distance between two consecutive leads in this image is 10 μm and each lead has width of 1μm.

the acetone. Once wire part was made, the same precedure was followed for the leads. Just before the evaporation, very small amount of developed area, usually less than 1 nm, was etched using VEECO 3 cm 1 keV Ar-ion beam (etch rate of approx. 0.1 nm/sec with gas pressure of 4.0×10^{-4} mB) to get rid of possible oxidized layer formed over the surface of Py wire during the preparation steps for the second lithography to improve the contact between Py wire and Au leads. 40 nm of Au (deposited at the rate of 0.2 nm/sec) was used for the leads with 1.5 nm of Ti (deposited at the rate of 0.1 nm/sec) as an adhesive layer. An example of resultant pattern is given in Figure 3.1.

Four different size of Py wire samples were fabricated and tested and the sample parameters are given in Table 3.1.

Table 3.1: Samples used in magnetotransport and noise measurements. All samples are 10 nm thick permalloy, and each segment is 10 μm in length.

Sample	w [nm]	ρ(T=2 K) [$\mu\Omega$-cm]	AMR (2 K)	B_s [T]
A	27	44.86	3.1%	0.47
B	50	48.63	3.5%	0.63
C	100	50.87	3.8%	0.59
D	450	50.55	3.7%	0.34

3.1.2 $\mathbf{In_{1-x}Mn_xAs}$

Provided DMS films were grown on (100) GaAs wafers by molecular beam epitaxy (MBE), starting with highly resistive 500 nm AlSb buffer layers grown at a substrate temperature of 560 °C with a growth rate of 0.9 μm/h. Then, 20 nm $In_{1-x}Mn_xAs$ films were deposited at a substrate temperature of $\sim$ 200 °C and with a V/III flux ratio, $r = 3.4$. Mn concentration was kept $<$ 6 % in order to avoid the formation of MnAs second phase. Details of the MBE process are reported in a recent paper[52]. Cap layers were not added for easier electrical contacts. Films were put at 190 °C for two hours for annealing in air atmosphere, which reduces the number of interstitial Mn donors and increases the hole density. This consequently improves their magnetic properties. Prepared in this manner, the magnetic easy axis of the $In_{1-x}Mn_xAs$ is along the growth direction.

Two different films were used to fabricate identically shaped wire samples. Samples were negatively patterned by standard electron beam lithography. Hence, after development, parts on the surface other than the actual desired pattern shape would be exposed. Once developed, a 1 keV Ar-ion beam was used to etch away unnecessary parts of the film to generate the desired pattern as shown in Figure 3.2. AFM measurements on the processed samples show that the apparent unetched widths of the wire segments and

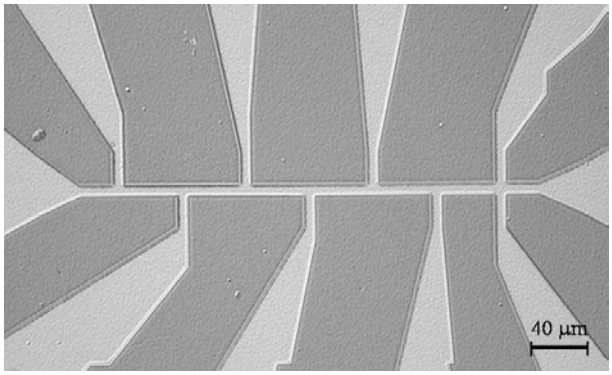

Figure 3.2: Sample image was taken using optical microscope. Brighter parts of the image are the remaining $In_{1-x}Mn_xAs$ layer. Darker parts are the exposed buffer layer after etching.

Table 3.2: Some parameters for both $In_{1-x}Mn_xAs$ samples used in the experiment are listed. Resistivity, carrier density and mobility are calculated from the sample resistance and the Hall resistance measured at 300 K, 3 T. All samples have wire part whose width is ~ 6.5 μm and thickness is 20 nm, and composed of six segments with length of 40 μm each.

Sample	x	T_C [K]	ρ [$\times 10^{-2}$ Ω cm]	p_v [$\times 10^{20}$ cm^{-3}]	μ [cm^2/ V s]
E	0.058	47	1.42	1.87	2.34
F	0.045	27	1.12	1.90	2.94

the narrow parts of the leads are ~ 6.5 μm, and the center to center distances between consecutive leads is 40 μm. Two aligned transverse leads on the right were purposely designed for the Hall effectmeasurements. Table 3.2 shows the specifications of the two samples. The resistivities for the processed material are several times higher than for the bulk films (3 - 5 mΩ cm). This suggests that the etching damages even the unexposed part of semiconductor, though the magnetic properties apper essentially unaffected by the etching.

3.2 Measurements

Once sample fabrication was finished, the sample was attached to a DC resistivity puck designed for insertion into a Quantum Design Physical Properties Measurement System (PPMS). The PPMS is an open cycle ^{4}He cryostat with a 9 T superconducting magnet. Samples were wired using uninsulated 99.99 % Au wire and indium solder joints.

All wire sample (Py and DMS) resistance measurements were carried on by a Stanford Research Systems model SR830 DSP Lock-in amplifiers. Output data from lock-in were then stored in the computer via Keithley 2000 Multimeter. Four terminal measurement scheme was used for resistive measurements for the characterization of the samples whereas for the noise fluctuation measurements, five terminal bridge scheme[53] was adapted to increase the sensitivity of the measurements. And for the noise measurements, signal from sample was fed into SR785 spectrum analyzer first from SR830 lock-in and converted into frequency domain before saving.

All the measurements described in the following subsections were performed twice for each wire sample - first with wire sitting perpendicular to the field direction and once again with wire's long axis (current direction) being parallel to the field.

3.2.1 Resistnace Measurements

Simple resistance, magnetoresistance and Hall effect were all measured using four terminal measurement scheme. The circuit schematics are shown in Figure 3.3.

A voltage source from SR830 lock-in with a ballast resistor, R_B was used to source a current to the sample from two outer leads with frequency set around 600 Hz. And the measured voltage difference from inner two leads were first preamplified using NF

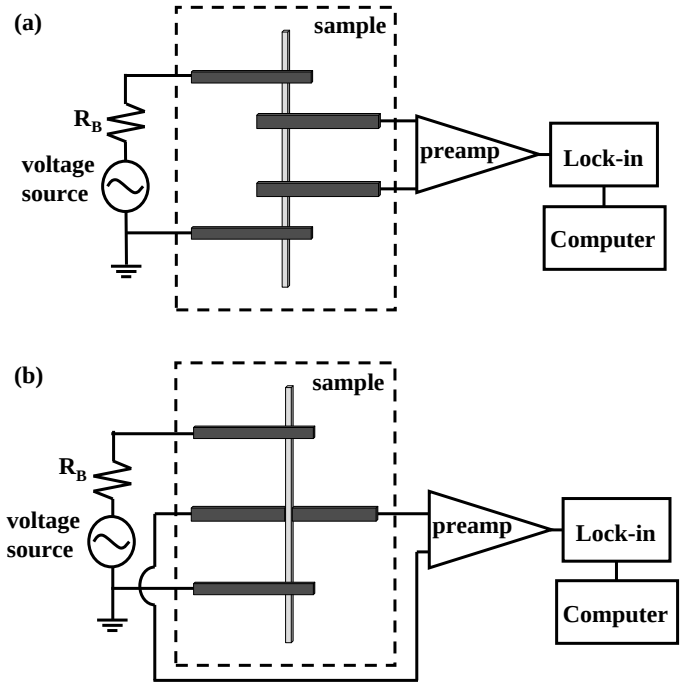

Figure 3.3: The ac four terminal resistance measurement schematics. (a) shows typical resistance measurements setup and (b) is for Hall resistance measurement setup. For both cases, dashed line box indicates sample area where the lighter color represents wire, and the darker color represents the leads.

Electronic Instruments LI-75 preamplifier and demodulated by the same SR-830 lock-in that was used for the voltage source.

Temperature dependence of the sample resistance with zero field were measured first from 300 K down to 2 K while changing temperature continuously. This initial measurement provides an important background information on what range of measurement sensitivities we could use for various temperature and magnetic field conditions since in our experiments, the sample arrangement is such that show resistance drop with 1) decrease of temperature and 2) applied external magnetic field.

After cooling was finished, the same setup was used to measure magnetoresistive effect. Magnetic field was applied perpendicular or parallel to the current direction varying continuously from - 9 T to + 9 T. Field sweeping speed was between 5 to 150 Oe/s, and at least one or more temperature sets were checked with more than two different sweep speeds to ensure the effect due to continuous sweep was minimized. For Py wire samples Hall effect was not measured, but for DMS wire samples Hall effect and magnetoresistive effect were measured simultaneously using two identical lock-in's whose lock-in frequencies were synchronized to one source. Data collection time was typically set to one second.

Finally, once all the measurements with perpendicular configuration (magnetic field applied perpendicularly to the sample surface) were done, all the same measurements were repeated in the exactly the same manner with the parallel configuration where the sample was reoriented so that the wire direction (current dirrection) was aligned to the external magnetic field direction.

3.2.2 Noise Measurements

The noise measurement requires a little more detailed explanation because the effect is small and other noise source within the measurement circuit can be restrictively large.

A typical dc four-terminal resistance measurement is known to have two major noise sources. One is the noise in the current source because ballast resistor will generate $1/f$ noise also known as pink noise when voltage is applied. The other one arises when measured signal is amplified. This is also pink. By using ac setup instead, the effective noise due to amplification becomes white noise. However, ac four-terminal setup is still sensitive to to fluctuations in the dirve current. The standard method to eliminate sensitivity to the drive current in resistance measurement is to use a bridge circuit such as Wheatstone bridge. All the noise measurements reported in this thesis was done using a modified Wheatstone bridge setup instead of conventional ac four-terminal setup.

Another merit of using the bridge setup is its sensitivity. Since the resistance of the sample is nulled out and the signal being measured is purely fluctuation related, measurement sensitivity can be set to the fluctuation size without being affected by the sample resistance which can be very large compared to the size of the fluctuations.

The modified bridge setup was first proposed by John Scofield specially to perform $1/f$ noise measurements in thin films[53]. Schematics are shown in Figure 3.4. The sample was center-tapped and each half was used as one resistor in the bridge. Two sets of variable resistor and variable capacitor are used to complete the bridge setup and null out the resistance, any measured fluctuations away from this null would be a result of sample noise.

Several other parts in the circuits should also be considered carefully since they could

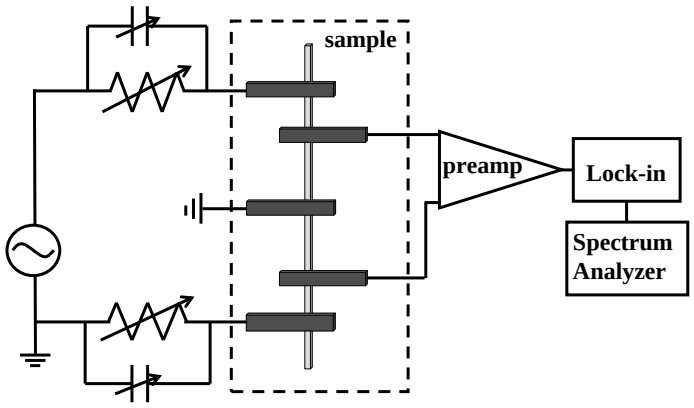

Figure 3.4: The ac five terminal bridge measurement schematics. Again, dashed line box indicates sample area where the lighter color represents wire, and the darker color represents the leads.

act as other possible noise sources. For the variable resistors, two General Radio 1433-H 10 MΩ decade resistors were selected . And to minimize the noise in the leads (contact fluctuations) fairly large resistance values were chosen for two variable resistors (typical settings were 1 MΩ). Variable capacitors were also added to this circuit for the phase matching purpose. It is because if the phases on both sides of bridge are mismatched it would result in lowering measured noise power. Drive frequency for the measurements was set to near 600 Hz since the preamplifier used in the circuit (an NF electronic instruments LI-75A low noise preamplifier) is optimized so that with much larger variable resistors compared to sample resistance the input impedence seen by the preamplifier is equal to the sample resistance.

The final signal from the output of the lock-in amplifier was fed into a Stanford Research Systems SR785 spectrum analyzer performed a fast Fourier transform (FFT) on the data so it could be observed in the frequency domain. The FFT bandwidth went

from 0 to 0.78 - 3.125 Hz depending on the size of the noise power.

Last one needed to be addressed is noise from preamplifier. Since all other unwanted noises can be taken care of by electronics setup, and both lock-in amplifier and spectrum analyzer can take in-phase and out-of-phase signals simulatneously, this extra noise can be treated quite easily. In fact, any noise recorded through out-of-phase channel after phase correction should be preamplifier noise and white noise, and the in-phase channel signal should be the sample noise plus this extra noise. Thus, sample noise can simply be calculated by subtracting out-of-phase channel signal from in-phase signal, and the resulting noise spectrum should be $1/f$ noise. Figure 3.5 shows a typical noise data.

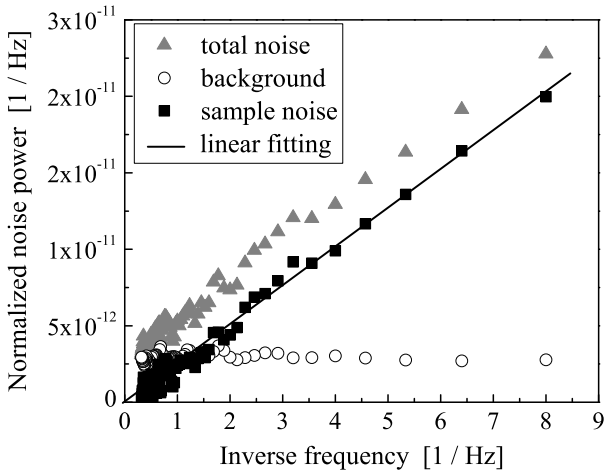

Figure 3.5: A typical noise power spectrum. The data was acquired from a 10 nm wide Py sample. Total noise indicates in-phase channel signal and background indicates out-of-phase channel signal.

The final data such as shown in Figure 3.5 were the results of averaging 90 to 120 spectra acquired one after another by SR785 (number varies depending on the sample). Data process was pretty simple once spectrum was acquired. $1/f$ sample noise was

calculated simply by substrating background noise (out-of-phase channel) from total noise (in-phase channel) then a straight line was fitted to $1/f$ plot to figure out the noise power for a given temperature and field setting.

The ac bridge scheme is also ideal for magnetofingerprint measurements. If a four-terminal measurement was used, measurement sensitivity would simply be dominated by comparably huge MR effects,especially around zero field region, resulting field dependent fluctuation almost impossible to resolve. However, because each half of the bridge will have a different magnetofingerprint even when the five-terminal setup effectively cancels out any magnetoresistive effect, field dependent fluctuations can be measured down to zero field. The only change made from Figure 3.4 was to take the spectrum analyzer out from the schematics so resistance fluctuations of the sample due to continuous field change could be recorded directly.

3.3 Results and Discussions: Permalloy

The goal of this measurements using FM materials was to understand the interplay between quantum coherence phenomena in a strongly correlated systems. In order to achieve this goal, we wanted to see 1) if there is any difference in results, such as effects due to the presence of domain walls, from that of normal metal samples as AuPd or Au nanowires, and if so, 2) the coherence length or time of a given system should be inferred out from using the similar method applied to normal metal systems.

Py is a relatively soft ferromagnet and geometric anisotropy strongly influences domain configurations, which makes Py a good candidate for testing the effects due to domain walls with relatively small magnetic field. And because of geometric anisotropy,

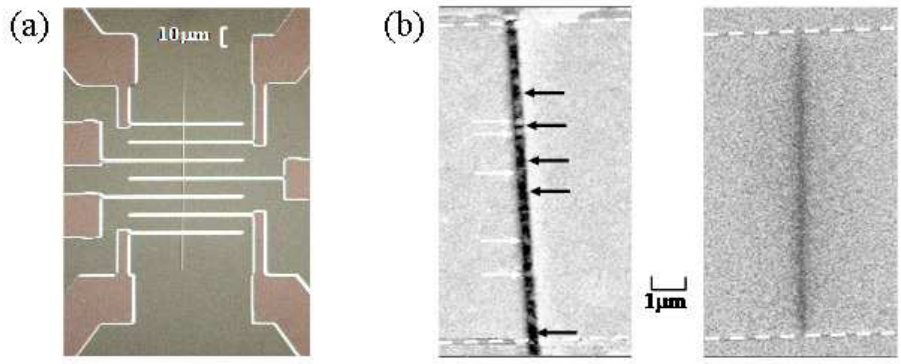

Figure 3.6: (a) Typical view of sample. Py wire was made first and 1.5 nm Ti/40 nm Au leads were added on top of the wire. Each of seven leads is 10 μm apart from the ajacent ones, hence forming six segments. (b) MFM image for one segment of two different Py wire samples (the left image is from 450 nm wide wire and the right is from 27 nm wide wire). Note that the wide wire (left) exhibits multiple domain features whereas narrow one maintains a single domain structure for fairly long range even at room temperature.

it is easier to control domain configuration simply by changing width of fabricated samples. Figure 3.6 shows magnetic force microscopy (MFM) images of two such samples after exposure to applied fields perpendicular to the wires. 100 nm or wider wires showed multiple domain walls within one segment, whereas long single domain features were observed for the smaller wires, with few domain walls throughout all six segments.

3.3.1 Resistive Measurements

Imaging their domain structures using MFM is one way of making sure that our sample has desired magnetic properties. However, there is also another way of checking sample's magnetic properties electronically before performing the noise measurement. That is, testing sample's magnetoresistance effects. As mentioned earlier, Py is known to show the AMR effect, which makes the magnetoresistive noise measurement significantly harder. However, the effect itself contains useful information of the sample's magnetization. A

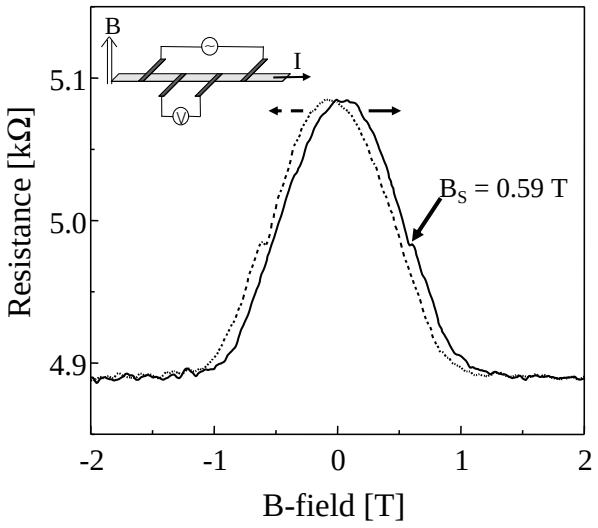

Figure 3.7: AMR data with a perpendicular magnetic field for the 100 nm-wide wire at 8 K. Field was swept between ± 2 T. Solid line is for sweeping the field from - 2 T to + 2 T and dashed line is for the other direction. Arrow points the discontinuity due to magnetization reorientation, and the swtiching field, B_s, for this sample at 8 K was ∼ 0.59 T.

typical AMR result for a 100 nm wide wire at 8 K with perpendicular magnetic field sweeping at 100 Oe/s between ± 2 T is shown in Figure 3.7. At low fields the geometric anisotropy leads the sample magnetization, $\vec{M}$ to align to the long axis of the wire and hence the current density, $\vec{J}$. At large fields, $\vec{M} \cdot \vec{J} = 0$, leads to a lower resistivity via the AMR (check chapter 1.6.2). All four samples showed a 3 - 4 % AMR resistivity (or resistance) ratio (check Table 3.1), R_Δ/R_0 agreeing with previously reported values on this material[17, 54].

One important point that needs to be mentioned is the discontinuity that occurs at the switching field, B_s, corresponding to reorienting unstable domains. When the applied field is much greater than the switching field, the magnetization, M, is believed to be uniform and aligned with the applied external field. This switching field value is

weakly temperature dependent, and becomes smaller from around 0.6 T at below 10 K down to 0.2 T as temperature raised to room temperature. As will be discussed again later, this switching field becomes important when the noise measurement was done at some nonzero fields. On top of the change in switching field values, shape of curves also gets narrower as temperature goes up. Both of which indicate the fact that at low temperatures magnetization, M becomes stiffer and harder to turn around with external magnetic field. The fact that there was no detectable WL magnetoreisstance down to 1.7 K should be noted as well. Since WL effect is strongly tied to the cooperon contributions, lack of WL effect suggests the suppression of cooperon in FM nanowire samples.

One other thing measured prior to noise measurement is the temperature dependence of sample resistance. In fact, $R(T)$ is the first measurement performed on every wire samples once they were placed in PPMS. The inset in Figure 3.8 shows typical temperature dependence of the sample resistance. A good Py wire sample shows a metallic behavior, which means the resistance of the sample decreases as temperature is lowered. However, when temperature goes further down below 15 K or so, the resistance starts to go up again due to electron-electron interactions in disordered system. Typically in a disordered metal system, electron-electron interactions are effectively screened at higher temperature, and resistance of the sample is dominated by phonons. As temperature goes down phonon contributions become substantially suppressed, and hence, the resistance of the system is lowered[10]. However, when the temperature is further lowered, the screening effect dies away progressively and thus, electron-electron interactions become more important. At low temperatures, the dominating electron-electron Coulomb interaction

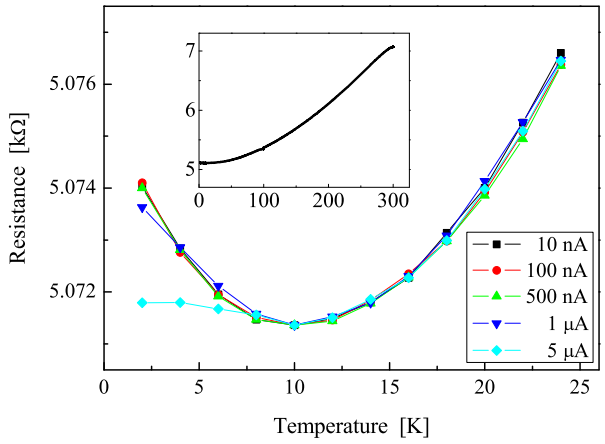

Figure 3.8: R vs. T below 25 K is shown for 100 nm Py sample (Sample C in Table 3.1). Resistance starts to show upturn below 15 K or so because boundary scatteringprocess becomes more prominant due to inceased coherence length of electrons. Several different drive currents were tested in ordered to minimize the problem with Joule heating. Inset shows $R(T)$ from 300 K down to 2 K.

creates a "migration" of electron states away from the Fermi energy. This lowered number of states coupled with the reduced thermal energy of the electrons results in fewer available states for conduction electrons to occupy, thus resulting increased resistance at lower temperature[55].

Now, the reason it is necessary to check $R(T)$ with various drive currents is because of Joule heating effects. Joule heating results from electrons colliding with defects transferring energy to them. At low temperatures, however, this transferred energy cannot be dissipated effectively since there are not many available phonons left in the system to distribute the heat at these temperatures. This makes the sample very poor at dissipating heat. Thus, if enough energy is given to the electrons by applying high enough drive currents, the resulting collision will actually increase the sample temperature, leaving the conduction electrons at a higher temperature than what thermometer claims. This

is highly undesirable as most of the coherence phenomena are strongly temperature dependent. Therefore, it is necessary to find the highest possible drive current that does not affect the sample temperature is crucial for the rest of the measurements follows here after. As shown in Figure 3.8 for 100 nm-wide sample as an example, maximum drive current that could be used for this specific sample at 2 K was 500 nA.

3.3.2 UCF Measurements

TD-UCF and MF-UCF (MFP) were measured using a five-terminal bridge setup with a suitable drive current for any given temperature found from $R(T)$ measurement. First of all, the noise power measured at low temperature was very well described by a $1/f$ dependence, and scales with the square of the drive current, indicating that its source is a fluctuating sample resistance. In fact, the frequency dependence remained $1/f$ for all samples and all parallel and perpendicular fields examined between 0 and 8 T, even when the magnetic field was very close to switching field, B_s.

Figure 3.9 shows noise power normalized by drive frequency and sample resistance as a function of temperature, $S_R(T)$ for all four Py wire samples under a variety of perpendicular field conditions. The fact that this noise is TD-UCF is supported by several reasons. Most importantly, the $1/f$ noise power *increases* as temperature is *decreased* for the low temperature region (below 50 T); this is expected in TD-UCF due to redueced ensemble averaging as k_BT decreases relative to the Thouless energy $\hbar D/L_\phi^2$, and $L_\phi(T)$ grows relative to the sample size, L. This is a unique, distinguishing feature of TD-UCF, and differs dramatically from *e.g.* local interference noise[33]. Second, the magnitude of the noise power increases with decreasing sample cross section, as is routinely

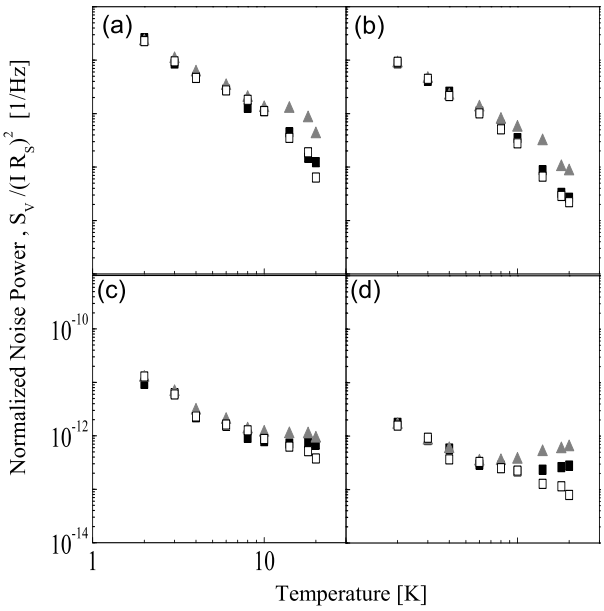

Figure 3.9: Noise power as a function of temperature for all four samples with several perpendicular magnetic field conditions: (a) Sample A ($w = 27$ nm), (b) 50 nm, (c) 100 nm, and (d) 450 nm. For all four sets of data, solid squares are $B = 0$ T; open squares are $B_\perp = 8$ T; and solid gray triangle is $B_\perp \sim B_s$. Size of error bars are comparable in size to the symbols.

observed in TD-UCF measurements of normal metals. Furthermore, the magnitude of the noise is comparable to that observed in TD-UCF measurements on a normal metal alloy, $Au_{0.6}Pd_{0.4}$, known to have a short coherence length.

It is already discussed that the field dependent suppression of the cooperon contribution to the noise power should be observed in normal metal was not observed in Py wire samples. As shown in Figure 3.9, no suppression was observed. For all four samples $S_R(B = 0)$ and $S_R(B_\perp = 8\ \mathrm{T})$ are almost indistinguishable within the temperature range tested. These data and the lack of detectable WL effect imply that cooperon are indeed suppressed in this material. This implies, unfortunately, that the field dependence of TD-UCF cannot be used to analyze L_ϕ quantitatively in this systems.

Even though it is disappointing that the coherence length cannot be inferred from the cooperon suppression, Figure 3.9 provides several interesting facts related to the coherence phenomena in this material. The noisepower data taken around the switching field, B_s are particularly interesting. Noise measurements were not possible precisely at $B_\perp = B_s$ due to large, irreversible fluctuations in bridge signal from domain rearrangements. Instead, noise data were acquired at fields 0.05 - 0.1 T away from B_s while sweeping $B \rightarrow B_s$. At these values of field and between 10 K and 20 K, S_R was observed to be enhanced relative to the single-domain case. Interestingly, the power spectrum of the fluctuators responsible for the noise continue to have a broad distribution of relaxation times (sample maintains its $1/f$ features). It is unlikely that this feature is related to magnetization reorientation and AMR effects, since simple AMR should be visible over all temperatures. Rather, these data support the idea that domain walls can act as coherent scatterers of electrons, and their motion can be a source of TD-UCF noise. The limited temperature range over

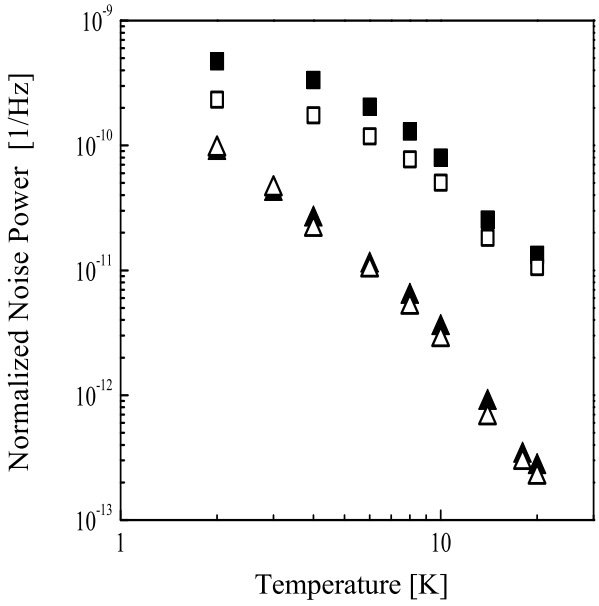

Figure 3.10: Comparison of noise power plot between 50-nm-wide Py wire (triangle points) and 35-nm-wide nonmagnetic samples (square points). Solid symbols are for zero field and open symbols are for $B = 0.512\ T$ for nonmagnetic wire and $B = 8\ T$ for magnetic wire. Nonmagnetic wire data were all shifted upward by a factor of 5 for clarity.

which these effects are measurable would then be determined by a combination of domain wall dynamics (magnetization must fluctuate on the slow time scales probed by the noise measurement) and the requirement of quantum coherence - as T increases, TD-UCF are increasingly suppressed because of thermal averaging and dephasing $L_\phi(T)$. More direct tests of these ideas should be possible, *e.g.*, in structures engineered to contain only a single domain wall[56].

Decoherence process may still be indirectly examined via $S_R(T)$. Figure 3.10 compares the temperature dependence of the TD-UCF noise power in the 50-nm-wide Py sample and a 35-nm-wide $Au_{0.6}Pd_{0.4}$ wire. The difference between low and high fields is

clear in the normal metal at low temperatures, while immeasurably small in the ferromagnets, again demonstrating the suppression of the cooperon contributions. Note that $S_R(T) \sim T^{-2}$ between 2 and 8 K for narrower Py wires. While the temperature dependence is slightly weaker in wider wires ($\sim T^{-1.4}$ for a 450-nm-wide sample), it is *always* appreciably steeper than T^{-1}. This differs significantly for dephasing mechanisms, as described below.

With some assumptions, $S_R(T)$ can be related to the coherence length $L_\phi(T) = \sqrt{D\tau_\phi(T)}$, where D is the electronic diffusion constant and τ_ϕ is the decohernece time. In normal metals, the predicted $S_R(T)$ depends on the relationship between several length scales: segment length L, width w, thickness t, the thermal length $L_T = \sqrt{\hbar D/k_B T}$, and $L_\phi(T)$. Also relevant is the density of active fluctuators, $n(T)$, in the material. In the usual TLS model, $n(T) \approx T$, and such TLS are apparent from the low-T acoustic properties of polycrystalline metals (see Ref. [57], Chap. 4). In a quasi-two-dimensionall (Q2D) system ($L,\ w >> L_\phi,\ L_T >> t$), the expected temperature dependence[40, 58] is $S_R \sim n(T)L_{\min}^2 L_\phi^2$, where $L_{\min}$ is the smaller of L_T and L_ϕ. In quasi-2D bismuth[58, 59], this TLS-based analysis leads to an inferred $L_\phi \sim T^{-1/2}$, exactly as expected for electron-electron dephasing in 2D. For the normal metal data shown[44], the observed saturation of S_R at low temperatures is consistent with weak localization and TD-UCF measurements on this sample that indicate the presence of magnetic impurities in the AuPd and a resulting $L_\phi(T)$ saturation.

It is likely that the relevant fluctuators in the FM away from the switching field are the same TLS as in normal metals and hence would have the same $n(T)$. The lack of field dependence shows that the dominant fluctuators are *not* moving domain walls or glassy

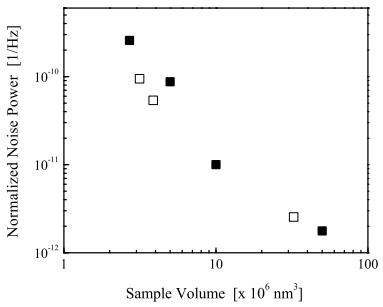

Figure 3.11: Noise power as a function of sample volume at 2 K. Solid squares are for Py wires and open squares are for nonmagnetic AuPd wires which have an identical sample geometry with thickness from 6.5 nm to 9 nm.

spins[60, 61].

Furthermore, the Figure 3.11 shows that S_R scales with sample volume identically in normal metals (AuPd) and the permalloy. Finally, the $1/f$ dependence of S_R is identical between AuPd and Py, showing that the fluctuators in both material systems have identical distributions of relaxation times. While not definitive, these observations and the ubiquitous presence of TLS in a variety of polycrystalline metals[57] suggest that it is reasonable that such fluctuators are active in the FM materials.

The dimensionality of Py wires with respect to coherence phenomena is remains unclear, though the most likely dimensionality is quasi-2D. A reasonable estimate for D based on the known values for iron and nickel suggests that $L_T \sim 10$ nm at 10 K. AB measurements in Py rings[50] at 30 mK estimate $L_\phi \sim$ hundreds of nanometers, and is *much* shorter at 4.2 K. L_ϕ values between 2 K and 20 K shorter than sample thinknesses or much larger than sample widths seem incompatible with these AB observations.

If $n(T) \sim T$ in these FM samples as in normal metals, then the implications for $L_\phi(T)$ are interesting. The unusually steep $S_R \sim T^{-2}$ is stronger than that expected

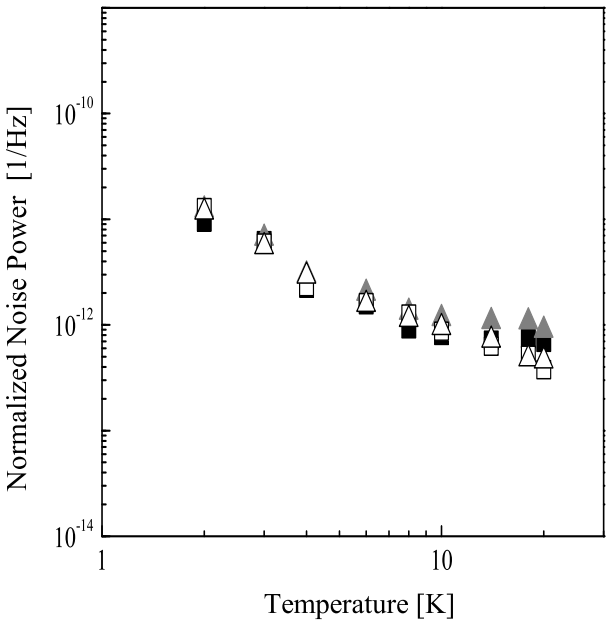

Figure 3.12: Noise power as a function of temperature for 100-nm-wide sample data from Figure 3.9 is revisited with parallel field data added to the plot. Open triangle represents data collected with 8 T magnetic field applied parallel to drive current direction. All other size samples showed simliar trend when parallel field was applied.

in *any* dimensionality assuming stardard electron-electron dephasing. Furthermore, the identical temperature dependences of S_R for low and high parallel magnetic field $B_{||}$ (check Figure 3.12) are inconsistent with spin wave scattering[62] as the dominant decoherence mechanism, since high $B_{||}$ is expected to exponentially suppress such mechanism.

3.4 Results and Discussions: $\mathbf{In_{1-x}Mn_xAs}$

Study of UCF noise in FM metal systems helped extending our understanding in QTP in FM systems. So it is logical to extend this idea to other types of FM materials.

In ferromagnetic semiconductors (FSs), carrier-mediated spin exchange between Mn ions is thought to be the origin of the FM phase. This is very different from that of FM

metal systems such as Py. The similar measurement techniques that were used for Py wire samples were used for FM samples and the results are discussed in this section. Two different batch of films were used to make identically shaped wire samples used in this experiments.

3.4.1 Resistive Measurements

As discussed in the previous chapter, $In_{1-x}Mn_xAs$ is paramagnetic above Curie temperature T_C and usually have relatively low T_C (typically between 10 and 100 K depending on various fabrication conditions). Therefore the most important thing that needed to be clarified is where exactly this Curie temperature lies.

A simple way of figuring out T_C with electrical setup is to measure the temperature dependence of the longitudinal and Hall resistance. At higher temperature, resistance of samples show increase of resistance as T decreased. This is a typical behavior for semiconductor. However, as seen in Figure 3.13 (a) and (c) the resistance (resistivity) of both samples peaks, indicating paramagnetic to ferromagnetic transition at T_C between 30 and 50 K while cooling, and this transition is more clear in the Hall resistance shown in Figure 3.13 (b) and (d), which exhibits ferromagnetic hysteresis for $T < T_C$ (gray lines). This is more pronounced as T is further reduced (black lines). Temperature range where TD-UCF and MF-UCF were measured was well below T_C so samples exhibited FM properties.

There are other test that can be performed in order to find out sample's magnetic properties, such as measuring magnetoresistive effects. As mentioned, magnetization easy axis for this samples lie along the film growth direction, which means the easy axis is the

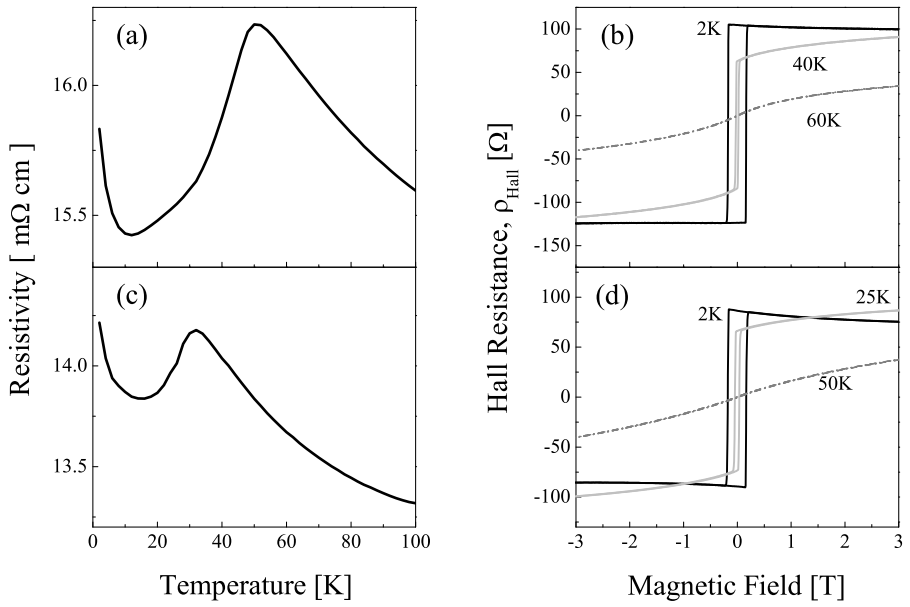

Figure 3.13: (a) Resistivity of sample E shows its Curie temperature around 50 K. (b) Hall resistance measurement for sample # 1 at 60 (dashed line), 40 (grey line), and 2 K (black line) shows appearance of magnetic hysteresis as cooling, which suggests the sample is experiencing paramagnetic to ferromagnetic transition. (c) Resistivity for sample F shows its Curie temperature lies $\sim$ 30 K. (d) Hall resistance for sample # 2 at 50 (dashed line), 25 (grey line) and 2 K (black line).

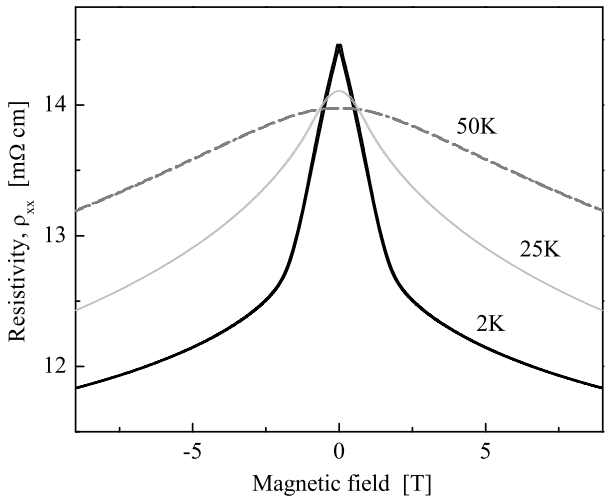

Figure 3.14: Magnetic field dependences of sample resistivity at three different temperatures are shown for sample F.

out-of-plane direction. Hence it is easier to see the magnetoresistive effect of these devices if the sample is rotated so the wire is parallel to external magnetic field. Figure 3.14 shows the development of magnetoresistive effect in sample F as the temperature goes down with magnetic field applied parallel to the sample plane. At $T > T_C$ no obvious MR can be seen whereas at T well below T_C it shows unmistakable sharp MR feature emerged.

3.4.2 UCF Measurements

The frequency dependence of the raw voltage noise power is well described as $1/f$ just like Py sample case. And again, the *increase* of noise power as T is *decreased* is a unique, distinguishing feature expected in TD-UCF noise (Figure 3.15, and results from the growth of the cohernece length, L_ϕ as discussed previously. Above ~ 5 K at $B = 0$ as well as over the whole temperature range for the high field data, the noise power varies approximately as $T^{-0.5}$. In the low temperature limit, the noise power scales

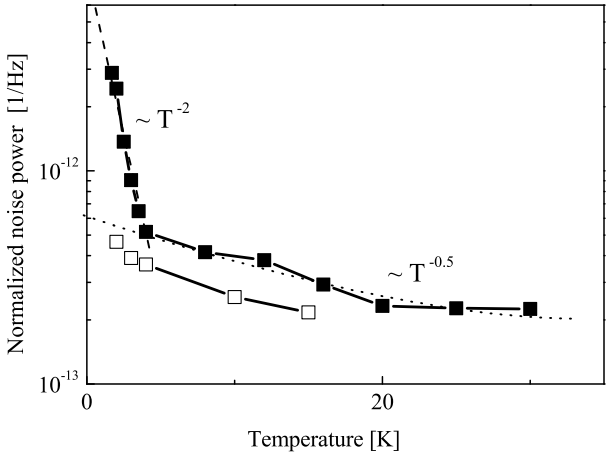

Figure 3.15: Normalized noise powers as a funcion of temperature for sample F at zero field (closed symbols) and $B = 3$ T (open symbols) are shown. The same trends are seen in sample E.

approximately as T^{-2}. Both of these dependences differ from the temperature dependence seen in nonmagnetic metals[40, 58]. These unusual temperature dependences suggests either 1) the fluctuators have an unusual energy distribution despite having the usual distribution of relaxation times that gives $S_R \sim 1/f$; or 2) the dephasing mechanism for holes in this material is unconventional.

Figure 3.16 shows the external field dependence of the TD-UCF noise power, $S_R(B)$, measurements on the two samples. In this plot, perpendicular and parallel field configurations are presented together with closed and open symbols, respectively. As shown in Figure 3.16, $S_R(B)$ in $In_{1-x}Mn_xAs$ system at low temperature is strikingly different to not only that of normal metals but also that of Py samples. And this strongly implies that the dominant source of TD-UCF is coherent scattering of carriers off fluctuating magnetic disorder. Qualitatively similar effects have been seen at mK temperatures in magnetic semiconductors that are considered as spin glass systems[63]. Above 5 K, S_R

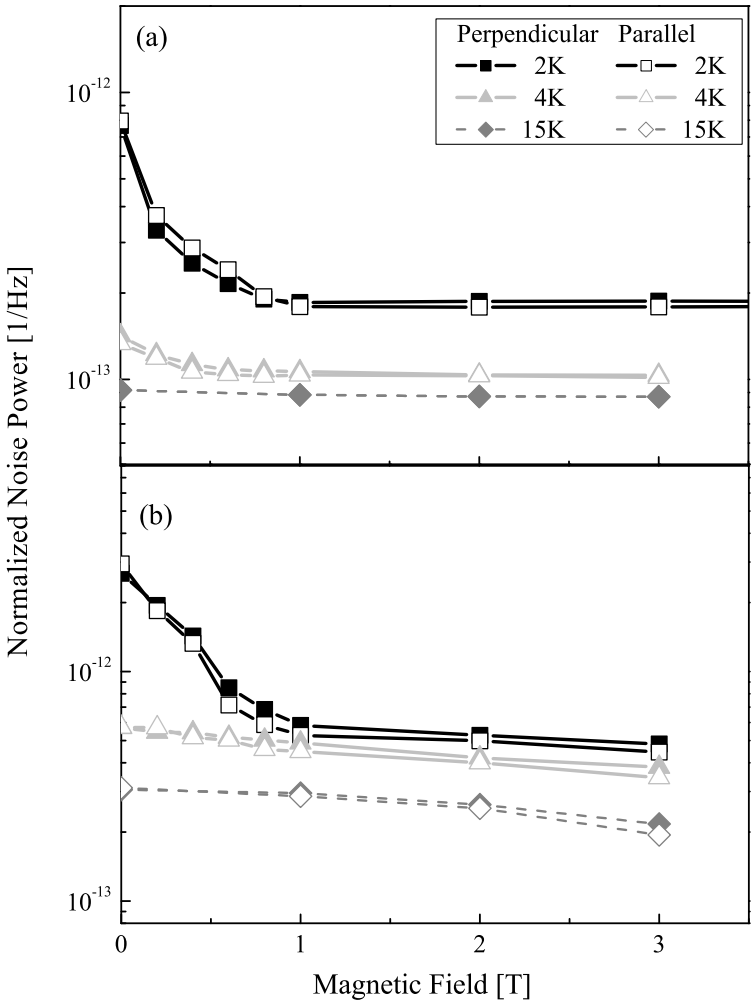

Figure 3.16: Normalized noise powers as a funcion of external magnetic field for (a) sample E, and (b) sample F are shown at three different temperaures, 2 K (black lines), 4 K (light gray lines), and 15 K (dashed gray lines). The closed symbols are for perpendicular configuration, and the open symbols are for parallel configuration. Error bars are not shown in these plots because they are comparable to the symbol size.

is independent of B, as seen in the Py experiments. However, as T goes below 5 K, S_R acquires a field dependence for $|B| < 1$ T. For both samples, $S_R(B = 0)$ becomes almost four times larger than $S_R(B = 1\text{T})$ at 2 K. As shown in Figure 3.16, this field dependence is independent of field orientation. This is consistent with a field-driven Zeeman suppression of the fluctuators that cause the noise, rather than an orbital coherence effect as in TD-UCF in normal metals.

In case of DMS samples, MF-UCF provides a consistency check on the idea that Zeeman rather than orbital physics is relevant to $S_R(B)$. Since Aharonov-Bohm shifting of phases of electronic trajectories is equivalent to altering the impurity configuration[38], sweeping B leads to sample-specific, reproducible MF-UCF within a coherent volume. The correlation field scale of the fluctuations, B_c, is related to the size of typical coherent trajectories via the flux quantum, h/e. Figure 3.17 shows MF-UCF for sample E in three different temperatures 2, 4, and 10 K from B = - 9 to 9 T when sample lies in perpendicular configuration. The symmetry in B abour $B = 0$ outside of the hysteretic portion of the conduction response confirms that these fluctuations are real. Qualitatively similar MF-UCFs occur in sample F. Note that the MF-UCFs reproduce when B is swept up and back. We assume a quasi-2D response, $B_c L_\phi^2 \sim h/e$, and check for consistency. While far more fluctuations are required for a firm quantitative estimate, Figure 3.17 (b) suggests that B_c at 2 K is on the order of 2 T, which would imply coherence length, $L_\phi \sim 50$ nm, larger than sample thickness as required for self-consistency. A truly quasi-2D sample would exhibit weaker fluctuations in the parallel configuration, and this is consistent with Figure 3.17 (c) and (d). The MF-UCF variance varied like $\sim T^{-4}$ dependence below 4 K, stronger than the TD-UCF variance, though statistics are poor

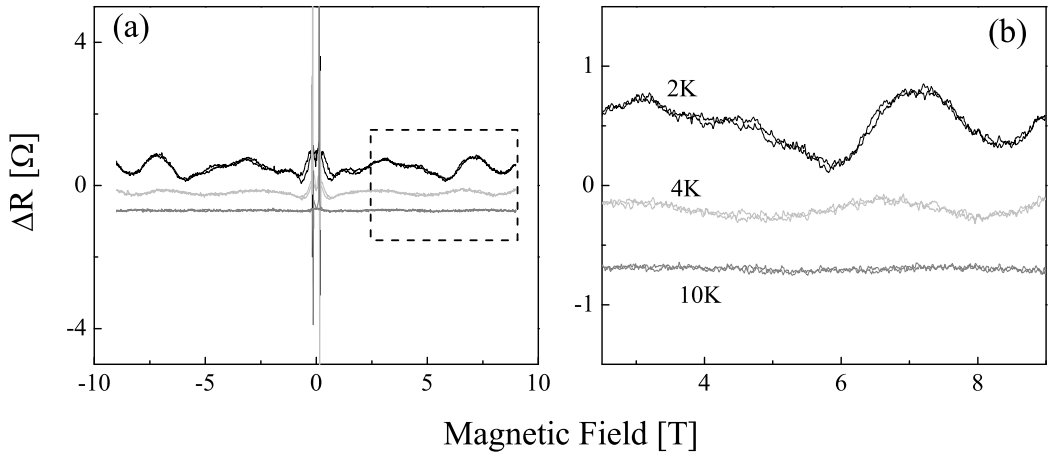

Figure 3.17: MF-UCF for sample E is presented at three different temperatures 2, 4, and 10 K for (a) perpendicular and (c) parallel configuration. (a) and (c) show full range of field sweep from -9 T to 9 T, and (b) and (d) are zoomed-in version for the marked area in (a) and (c), respectively.

because the apparent field scale of the MF-UCF is so large[64].

One possible origin of the TD-UCF in this material is that the fluctuators are associated with Mn spins, perhaps at the edges of the sample, not fully participating in the bulk FM order of the system. Coherent scattering off slowly fluctuating local magnetization could cause TD-UCF, as in the spin glass case[63]. At sufficiently large B those moments would be saturated, removing that source of fluctuations.

Chapter 4

Magnetite

While this part of research is focused on a completely different problem from the previous research with nanowires, the main concern is still the same: understanding electron transport under the influence of strongly correlated electron system. Magnetite, the most famous naturally occurring ferrimagnet (also widely mistaken as a ferromagnet to many) is chosen for that purpose. What makes magnetite material more interesting other than its magnetic properties is that magnetite has known to exhibit a sharp "bad" metal to insulator transition at $T \sim 122$ K, called Verwey transition. It is classified today as the occurrence of a spontaneous, intercorrelated change of both lattice symmetry and electric conductivity in certain ionic crystals. Typically, such an abrupt change is accompanied by further anomalies in a series of related parameters controlling the magnetic, thermodynamic, electric, and mechanical interactions in the solid[1, 65, 66, 67]. Thus it provides us many alternate means to test the sample. Since first discovery[24], Verwey transition related physics has been studied widely. However, most of experiments were carried on at a macroscopic scale using bulk material. Although there are certain merits in performing an experiment at larger scale, it is undoubtable that using nanoscale devices can be advantageous for understanding the changes in electronic states when the material undergoes this transition. Thus, a two terminal nanojunction setup was adopted.

4.1 Fabrications

Unlike nanowire samples which were patterned into simple wire shape to define the region of interests along with multiple leads attached to it to perform multi-leads electrical measurements, nanojunction devices were patterned in a simpler shape to further narrow down the region of interests. Two-terminal devices for applying voltages and measuring conduction at the nanoscale have been fabricated incorporating both Fe_3O_4 nanocrystals[68] (10-20 nm in diameter with oleic acid coating) and single-crystal thin films (40-60 nm thick)[69].

Even though it is still challenging from conventional techniques to fabricate a set of electrodes whose separation is comparable to the size of nanostructures, recently proposed approaches made this possible with a relatively high yields. Some of such approaches include nanopore structures[70, 71], employing scanning tunneling microscopy (STM)[72, 73, 74, 75, 76, 77] and electromigrated break junction[78, 79, 80, 81, 82, 83, 84]. However, in our experiments, conventional lithography defined structures were used due to some limitations other approaches have.

4.1.1 Nanocrystal Samples

Two-step electron beam lithography and e-beam evaporation (1 nm Ti, 15 nm Au) were used to pattern closely spaced source and drain electrode pairs onto degenerately n-doped silicon substrates coated with 200 nm of thermally grown SiO_2. Interelectrode gaps (channel lengths) ranged from zero to tens of nm, with a 10 μm wide channel region. Nanocrystals were spin-coated from hexane solutions to form slightly more than one densely packed monolayer of nanocrystals over the channel region. Samples were then

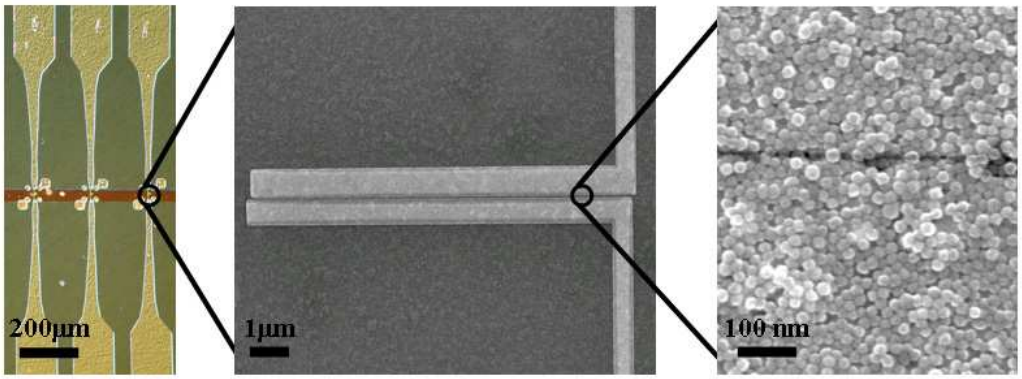

Figure 4.1: Au (no Ti) was used for the electrodes. Each device has channel width of 20 μm and channel length of 10 to 100 nm.

Magnetite nanocrystal preparation starts with the generation of iron carboxylate salts through dissolution of FeO(OH) in oleic acid. Then the decomposition of iron carboxylate salts results magnetite nanocrystals. This is a simple one pot process where you add FeO(OH) with oleic acid in a big mixer and heat everything up under various inert gas environment to around 320 °C for some fixed time[68], which results the desired final products. Size of nanocrystals can be regulated from several nm to hundreds of nm during the synthesis by adjusting the amount of oleic acid added to the process. Equation 4.1.1 shows a simplify version of the chemical equation for this process.

$$\mathrm{FeO(OH)} \ + \ \mathrm{OA} \ \xrightarrow{\Delta} \ \mathrm{Fe(OA)_3} \ + \ \mathrm{H_2O} \uparrow \ + \ \mathrm{ODE} \ \overset{\Delta\ 300^{\circ}\mathrm{C}}{\longrightarrow} \ \mathrm{Fe_3O_4\ nanocrystals} \tag{4.1.1}$$

The nanocrystals have been characterized by transmission electron microscopy (TEM), x-ray diffraction, and infrared and Raman spectroscopy. As synthesized the nanocrystals are protected by weakly bound oleic acid ligands; these ligands play a crucial role on regulating final size of nanocrystals during chemical synthesis and also allow the suspension of the nanocrystals in organic solvents, but act as electrically insulating layers that must be largely removed for effective electronic transport measurements. Thus, comes the baking procedure discussed earlier.

4.1.2 Thin Film Samples

The other type of devices are based on 50 nm thick epitaxial magnetite films grown by oxygen-plasma-assisted molecular beam epitaxy (MBE) on <100> MgO single-crystal substrates. Details of the growth process have been reported elsewhere[69]. Single-step e-beam lithography and e-beam evaporation were used to pattern Au (no Ti adhesion layer) source and drain electrodes defining a channel length ranging from tens of nm to hundreds of nm, and a channel width of 20 μm. The interelectrode conduction is dominated by the channel region due to this geometry. No annealing was performed following electrode deposition.

4.2 Measurements

After the fabrication, the samples were placed in ^{4}He cryostat fridge described earlier or a variable temperature vacuum probe station (Desert Cryogenics) for the electrical charicterization. When sample was placed in the probe station, the chamber was evacuated by a turbomolecular pump, preferrably overnight, and when the pressure went below 10^{-4} mBar, an inline cold trap is filled with liquid nitrogen for cryopumping. The base

pressure of the probe station at 300 K was 2 - 4 $\times$ 10^{-7} mBar. For all measurements, HP 4155A Semiconductor Parameter Analyzer was used except for the switching speed test.

During the initial cooling to liquid nitrogen temperature, resistance of each device was measured. All resistance values of the device were obtained from IV curves measured using parameter analyzer to source relatively small voltage upto 100 mV with step size of 5 mV. These initial resistance measurements provided important information about sample configurations. Due to a certain amount of inconsistency during the lithography procedure, devices ended up with non-regular gap sizes - some devices with too large or too small gaps and even no gaps for other devices. Plus, the placement technique for nanocrystals was less than optimal, relying largely on statistical chances. Thus, it was essential to find out which devices were worthy of close examination at lower temperature at an earlier stage. After processing large number of devices, we concluded that the ones that had the room temperature resistance of several kΩ or smaller showed interesting features at low temperatures. In case of larger resistance devices, it was very likely that the electron transport was dominated by large contact resistance due to poor coupling to electrodes or by large tunneling resistance due to large gap size. In any cases, the IV features we were interested in would not be appear. If two electrodes were connected, electron transport would be dominated by the path provided by touching electrodes, so again, the features from magnitite samples would not arise.

Figure 4.2 (a) shows three resistance vs. temperature trends nanocrystal devices usually follow. Type I devices with metallic behavior were considered to have connected electrodes, type II devices with relatively large room temperature resistance were considered to have larger gap sizes or large contact resistances, and type III devices which

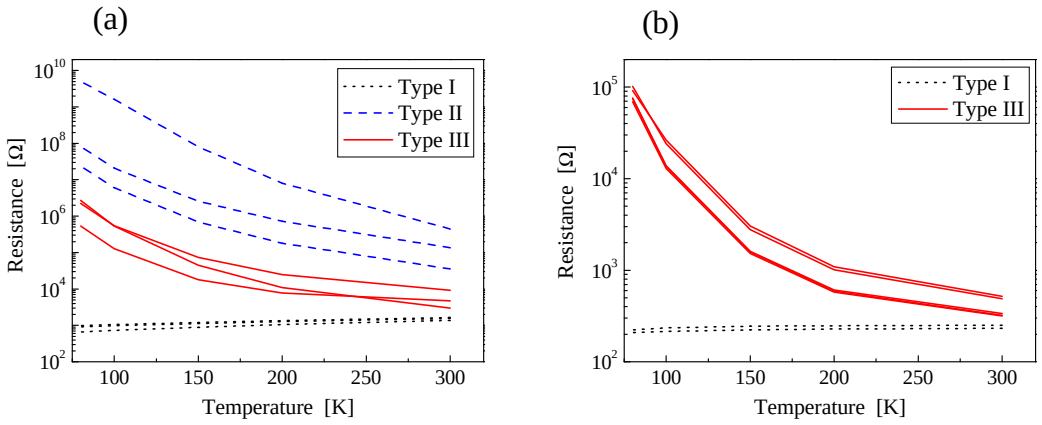

Figure 4.2: General trends of resistance vs. temperature plot in log-linear scale for (a) nanocrystal devices and (b) thin film devices.

showed interesting features at lower temperature were the ones considered to have optimal gap sizes and low contact resistance.

Although there was no device with too large a resistance in thin film samples, there were a few devices with connected electrodes. Therefore, even when thin film samples were tested, high temperature resistance measurements were still necessary. As seen in Figure 4.2 (b), thin film devices generally exhibited lower resistance values due to improved contact and well defined sample stoichiometry compared to nanocrystal devices. However, their temperature dependence followed similar trend.

Once interesting devices were identified, their IV characteristics were measured. Typical voltage range was between -2 V and +2 V though this range entirely depended on gap sizes as well as how good a contact resistance was. Step size was selected to accommodate the maximum number of data points parameter analyzer could take. And the voltage sweep was typically set to start at -2 V upto +2 V then brought back to -2 V

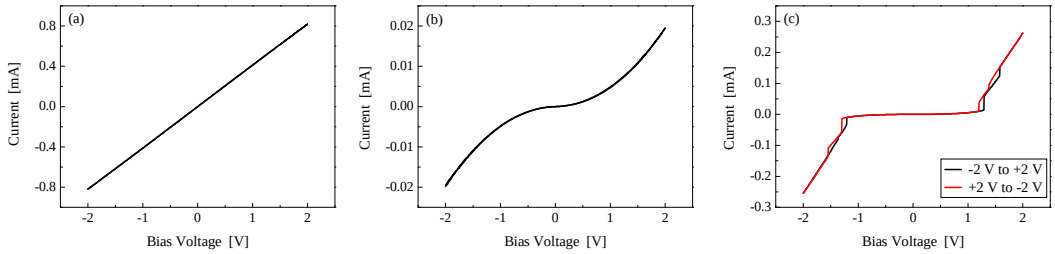

Figure 4.3: Three typical IV curves observed at 80 K with (a) metallic (connected electrodes), (b) insulating (too large a gap or poor contact) devices, and (c) with devices showing switching behavior at low temperature.

so we could observe electric field induced hysteretic effect below 120 K. Figure 4.3 shows three distinctive IV curves that might be seen at 80 K.

For the switching speed tests, the parameter analyzer was replaced by a Stanford Research Systems DS345 Function Generator to source the desired voltage range and a National Instruments BNC-2110 DAQ card to collect output current data converted into voltage using Stanford Research Systems SR570 current preamplifier. By using this setup, voltage sweep speed within the interested range could be controlled arbitrarily fast or slow depending on the frequency settings on the function generator.

4.3 Results and Discussions

As described in the previous section, resistance of all devices were tested during the initial cooling in order to select out which would be suitable for the further detailed measurements. The ideal profile of resistance as function of temperature would have been the ones showing sharp transitions across Verwey transition temperature at around 120 K[24, 1]. However, because of the limitations of two terminal setup, it is not avoidable to have the contact and lead resistances included to the total resistance measured, which could

dominate the overall resistance trends. In fact, if the known bulk resistivity of magnetite is used simple Ohm's law calculation gives the sample resistance should be low as 5 - 10 Ω in room temperature. Even though this is only a rough estimate this suggests that the total sample resistances measured were strongly dependent on the contact resistances. And unfortunately, that is true in many cases with two terminal devices. This is especially problematic with nanocrystal devices because nanocrystal is initially covered with oleic acid which must be eliminated. There is a higher chance some residues left behind causing bad contacts. So the selection process can be tricky sometimes. Nevertheless, the $I-V$ characteristics of well established nanojunction devices for both nanocrystals and films showed unmistakably clear features below Verwey transition temperature which will be described in this chapter.

4.3.1 Electrically-Driven Transition: Not Local Heating

Figure 4.4 shows $I-V$ and dI/dV characteristics of a nanocrystal device at some selected temepratures. For $T > T_V$, $I-V$ curve showed simple monotonous response to applied voltage (Figure 4.4 (a)). However, as the temperature was reduced, a discontinuity in $I-V$ curve started to develop (Figure 4.4 (b) and (c)). This is a feature certainly not present when gaps with no particle were put to test. Although the development of this switching effect under the change of temperature seems rather gradual, the fact that devices which showed this voltage driven transition in their $I-V$ curves all started to exhibit this transition only when the temperature is around or below 120 K strongly suggest the fact that this is related to the Verwey transition. Also, this was not just a case for nanocrystal magnetite samples but also for the MBE grown film samples with

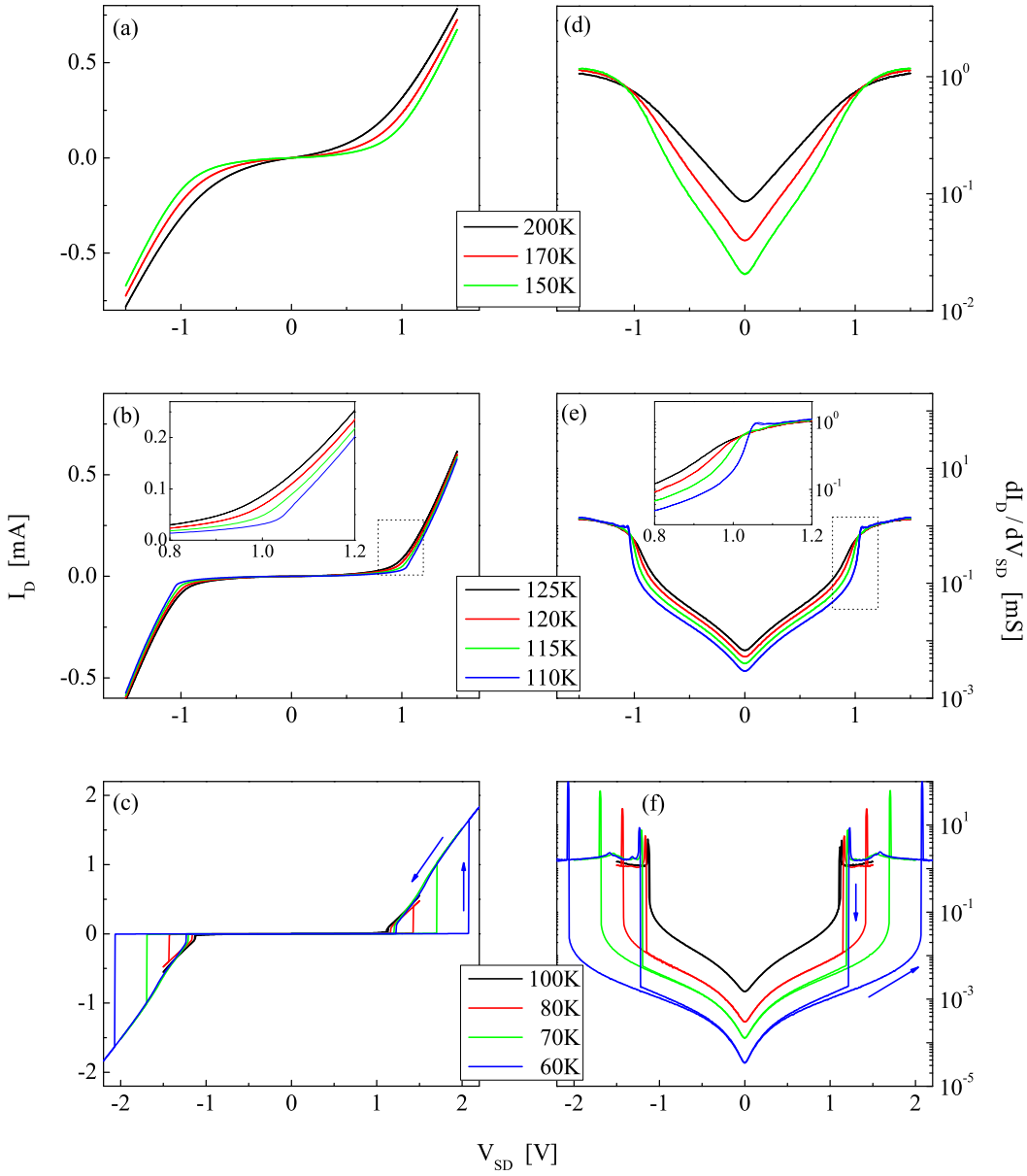

Figure 4.4: Current-voltage characteristics at various temperatures for a device based on 10 nm magnetite nanocrystals. (a) shows $I-V$ curves observed at temperatures above T_V. $I-V$ curves in (b) were measured more tighter range of temperatures around the Verwey transition. Inset is zoomed-in version for the marked area. The ones showed in (c) were from lower temperatures. Arrows indicate the direction of the hysteresis for 60 K data. (d), (e), and (f) are dI/dV for (a), (b), and (c), respectively.

various gap sizes.

The emergence of the transition becomes more obvious in dI/dV plot shown in Figure 4.4 (d), (e), and (f). Inset in Figure 4.4 (e) clearly shows the emergence of discontinuity below 120 K, which develops to huge jump in $I - V$ curves at lower temperatures (Figure 4.4 (c) and (f)). In fact, when d^2I/dV^2 is plotted, it starts to show a hint of discontinuity feature development at high as 150 K.

First and probably the most important part that requires further clarification is whether this voltage driven transition from low conducting state to high conducting state is due to local heating or not. We believe there are several evidences indicating these sharp conductance transitions are *not* the result of local heating (as in macroscopic samples of Fe_3O_4[85, 86] and in the Mott insulator VO_2[87, 88]), but rather are electrically driven. In the worst-case scenario, all of the $I \times V$ Joule heating power is dissipated within the magnetite. The local steady-state temperature is determined by the power dissipated and the thermal path. Thermally driven switching would then correspond to raising the *local* temperature above T_V. At a fixed cryostat temperature an improved thermal path would imply that more power dissipation would be required for a given local temperature rise. Similarly, for a fixed thermal path, the necessary dissipated power for thermal switching would approach zero as $T \rightarrow T_V$. Furthermore, at a given cryostat temperature thermally-driven switching would imply that the power dissipated at the low-to-high conductance transition (needed to raise the local temperature to T_V) should be close to that at the high-to-low conductance transition.

The thermal conductivity, κ, of magnetite is dominated by phonons in this temperature range, and limited by phonon-electron scattering[89], even when $T > T_V$. As a

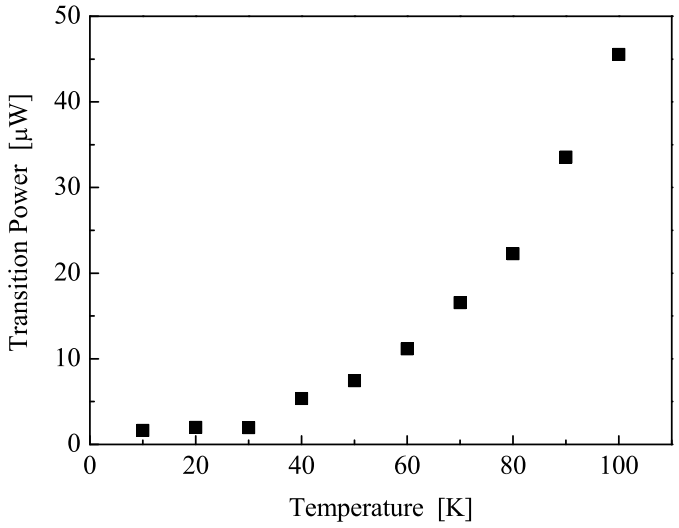

Figure 4.5: Power required to switch from the insulating into the more conducting state as a function of temperature, for a device based on $\sim$ 20 nm diameter nanocrystals.

result, κ increases as T is *decreased* through and below T_V, and the materials thermal coupling to the cryostat *improves* as T is reduced. In *all* devices showing switching, the electrical power required to switch from low to high conductance *decreases* with decreasing T, with Figure 4.5 showing one example. This is precisely the opposite of what one would expect from thermally-driven switching. Similarly, in all devices the power dissipated at switching does *not* approach zero as $T \rightarrow T_V$, again inconsistent with thermally-driven switching. Furthermore, at a given T the power dissipated just before V is swept back down through the high-to-low conductance threshold significantly exceeds that dissipated at the low-to-high point in many devices, including those in Figure 4.4, inconsistent with thermal switching expectations. Finally, nanocrystal and thin film devices show quantitatively similar switching properties (Figure 4.6) and trends with temperature, despite what would be expected to be very different thermal paths. These

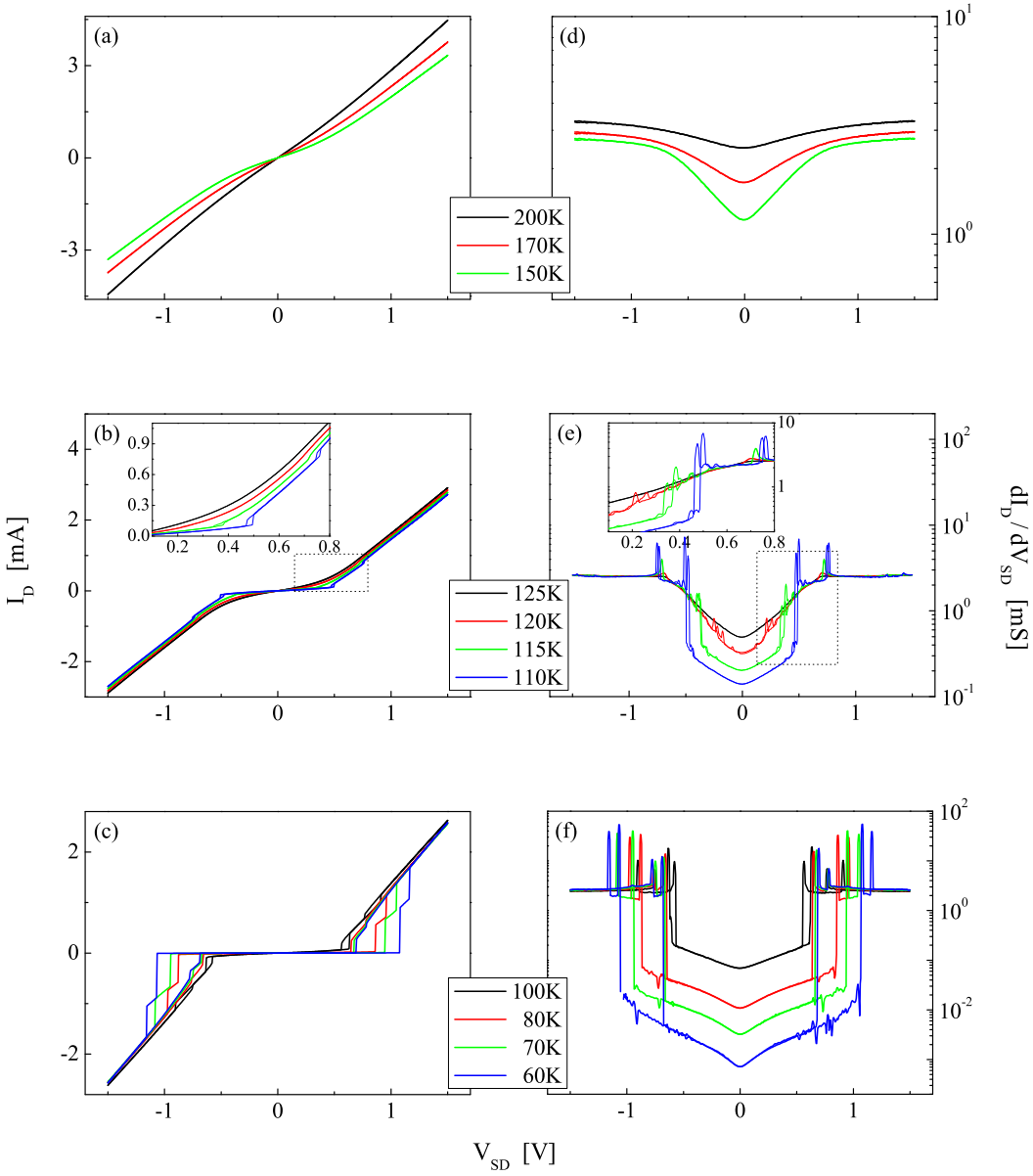

Figure 4.6: Current-voltage characteristics at various temperatures for a device based on 50 nm thick magnetite film grown onMgO substrate. (a) shows $I-V$ curves observed at temperatures above T_V. $I-V$ curves in (b) were measured more tighter range of temperatures around the Verwey transition. Inset is zoomed-in version for the marked area. The ones showed in (c) were from lower temperatures. Arrows indicate the direction of the hysteresis for 60 K data. (d), (e), and (f) are dI/dV for (a), (b), and (c), respectively.

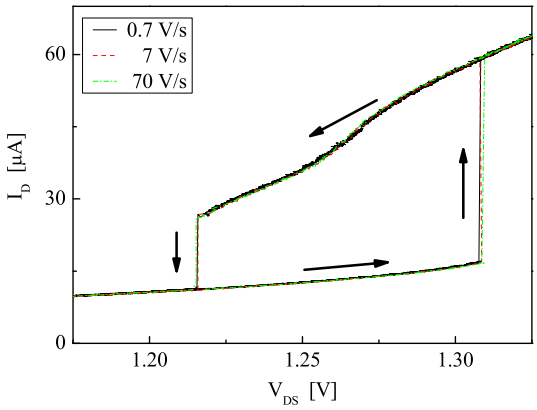

Figure 4.7: Hysteresis loops at various sweep rates on a nanocrystal device are shown. Voltage sweep rates were varied from 0.7 V/s up tp 70 V/s.

facts rule out local heating through the Verwey transition as the cause of the conductance switching.

4.3.2 More Details

As seen in both Figures 4.4 and 4.6, all conductance transitions below T_V are accompanied with hysteretic behavior depending on the voltage sweeping direction. These get more and more dramatic as T is decreased due to increase of threshold voltage for the switching. The transition in all devices are extremely sharp, with widths less than 50 μV, though in repeated sweeps at a fixed temperature, there is sweep-to-sweep variability of a few mV in switching thresholds. Furthermore, when tested with various sweep speed at a fixed temperature, the switching voltage and the sharpness of transition were maintained even with very fast (70 V/s) speed. This indicates that the switching process is relatively rapid. Figure 4.7 shows details of hysteresis loops on a nanocrystal device with various sweep rates.

The fact that the conductance transition is driven electrically can be also backed up

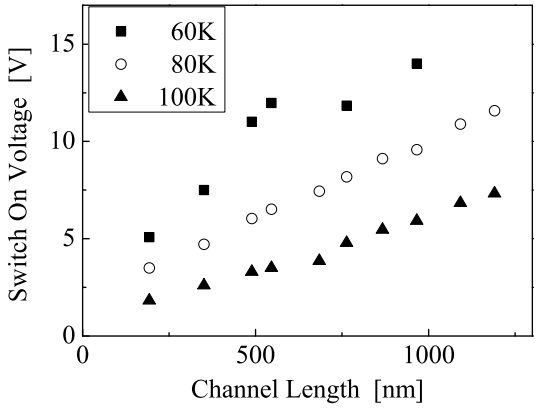

Figure 4.8: Switching voltage in a series of thim film devices as a function of channel length (gap size) at several temperatures. The linear variation with L strongly implies that for each temperature there is a characteristic electric field required for switching. The nonzero interception at $L = 0$ suggests presence of contact resistance.

by a plot of the low-to-high conductance switching volatge as a function of gap size L in a series of film devices for several temperatures (Figure 4.8). The linear dependence implies that the transition is driven by electric field itself, rather than by the absolute magnitude of the voltage or the current density. Tha fact that the voltage extrapolates to a nonzero value at $L = 0$ is likely a contact resistance effect. The length scaling of the transition voltage also demonstrates that this is a *bulk* effect. The contacts in all of these devices are identical, so any change in switching properties must result from the magnetite channel. This is contrast to the resistive switching in $Pr_{0.7}Ca_{0.3}MnO_3$ (PCMO) that is ascribed to a change in contact resistance due to occupation of interfacial states[90].

One of possible explanation of the switching features is that the nonequilibrium carrier distribution contributes to destabilizing the insulating state. In the presence of a strong electric field a carrier can gain significant energy even in a single hopping step, even though carrier relaxation times are very short. A rough estimate of the average critical

electric field for switching at 80 K is 10^7 V/m, from the slope of the line in Figure 4.8. The high temperature cubic unit cell is 8.4 Å on a side, meaning that a carrier traversing one cell would gain approximately 8.4 meV, comparable to $k_B T_V \approx 10.3$ meV. Conductance switching at such high fields may require consideration of such nonequilibrium carrier dynamics.

The gate and magnetic field dependences of nanocrystal devices were also tested. However, the switching characteristics were very much immune to any of those changes, possibly because of poor coupling between nanocrystal samples and the substrates used as a gate due to the same reason why some devices have bad contacts. Tested gate biases were between ± 80 V, and the field was brought up to ± 9 T. For both cases, voltage driven-transitions at lower temperature were still maintained with no obvious disturbance. Even with the case of underlying MR effect at high magnetic field, because of larger switching effect compared to MR effect, overall profile of the curve seemed unchanged at a larger scale.

Regardless of some limitations, we believe the electric-field driven transition seen in this material can serve us a new and important method of studying Verwey transition. On top of that, this also demonstrates that nanostructures of strongly correlated materials can lead to previously unknown physics which will help us in extending our understandings in such systems.

Chapter 5

Conclusion and Outlook

In this thesis, we investigated various types of magnetic materials to extend our understanding on electron transport in long-range, strongly correlated systems. For all samples, e-beam lithography was used in order to fabricate sample geometries that were sub-micrometer scales. Electrial measurements were used for both investigations of magnetic properties and of electron coherence.

5.1 Nanowires

For nanowire samples, initial measurements using conventional four-terminal setup demonstrated and varified samples' ferromagntic properties in the temperature range where our interest lies. Metallic nanowires (Py samples) showed typical negative magnetoresistance effect under varying magnetic fields with saturation field ranges around 1 T with fairly small switching fields at around 0.5 T suggesting its ferromagnetic properties as expected. In case of DMS samples, the MR effect and Hall effect measurements even showed distinctive development of ferromagnetism across the Curie temperature of the samples well above the temprature range that we are interested in.

TD-UCF measurements in two distinct types of materials provided several interesting aspects regarding magnetic ordering present in our samples. The suppression of cooperon contribution was one of the interesting outcome in metallic ferromagnetic samples. Other interesting results include: 1) domain wall motion as a possible scattering source[46] and

2) stronger temperature dependence of noise power which leads us to believe that there must be different decoherence mechanism compared to normal metal cases.

In DMS samples, noise power DID show certain field dependence. However, it does not appear to be cooperon contribution, either. Rather, it was believed to be due to field-driven Zeeman suppression. With DMS samples, MF-UCF was also closely examined. Even though the applied field was far from sufficiently large enough to be conclusive, the rough estimate of coherence length of this type of sample was possible.

It was rather unfortunate for both samples that quantitative results, for the coherence length, dominent dephasing mechanism and their temperature and/or field dependences, related to coherence physics were not obtained with ferromagnetic materials. Although the techniques adopted for this part of research was fully proven with non-magnetic metal systems, and existence of UCF noise in ferromagnetic samples was unmistakable, it was still not quite enough for the theories for non-magnetic metal systems to be fully compatible with ferromagnetic systems. However, we believe it was still possible to use this setup to have a better understanding.

There are several other types of experimental setup that could be used with some restrictions. The weak localization will be ruled out because of strong suppression of cooperon contributions. On the other hand, Aharonov-Bohm oscillation has been already shown to be useful to find the coherence length[31, 30]. There are also other attempts using superconductor-ferromagnet junction devices to find relavant coefficients that can be used to calculate coherence length of ferromangets in the system[91]. One of the down side of these experiments is that these experiments adopted rather complicated sample setup. However, in concert with other techniques, it should be possible to examine decoherence

in FM systems quantitatively, and search for other novel coherence effects[92, 93]. Plus, by continuing with other specifically ordered ferromagnetic samples such as DMS samples in our research, we believe more detailed understanding is still possible.

5.2 Magnetites

Simpler setup was used for magnetite samples in order to study electron transport in samples with further restricted geometry in this part of research. With magnetite nanocrystal samples, the initial objectives of the research was more oriented toward single molecular transistor type of experiments. However, the limitations related to sample fabrications, especially with the problem generally addressed as a contact problem(due to original nanocrystal sample fabrication methods as well as to our less than perfect placing techniques), sensitivity of conductance measurements, let alone with the lack of gating ability, was severely undermined. Instead, larger bias voltage regime was explored, and we were able to observe the electric field-driven transition below Verwey transition temperature.

We believe the field-driven conductance transition may give insights into the equilibrium Verwey transition. This switching may be useful in testing recent calculations[67, 94, 90] about the role of strongly correlated B site Fe 3d electrons and their coupling to phonons in the Verwey transition mechanism.

Along with field-driven transition, performing local probes of the magnetite structure (via x-ray or electron-diffraction techniques or scanned probe microscopy) *in situ* in the channel of biased devices would give an interesting insight. It would help us to understand if the coherence between structural symmetry changes and the formation of a gap in the electronic spectrum is broken under these noequilibrium conditions. However,

this is a significant experimental challenge. Similarly, local Raman spectroscopy of devices under bias could reveal field-induced changes in phonon modes and electron-phonon couplings, and single-crystal thin films permit the application of bias along well-defined crystallographic directions relevant to structural symmetry changes at T_V.

The presence of multiple switching transitions in individual nanocrystal and film devices also bears further study. The suggested charge order may melt inhomogeneously, with portions of the channel having different switching thresholds. There could also be charge-ordered intermediate states between the insulating regime and the most conducting regime[1]. Again, optical measurements[95] with sufficient spatial resolution could address these possibilities. Through improved metal/magnetite contacts and further study, it should be possible to unravel the precise nature of this nonequilibrium transition, and its relationship to the equilibrium, bulk Verwey transition.

5.3 Closing Remarks

There are many in condensed matter physics community considering the quantum transport physics in mesoscopic system, especially with disordered normal metal system, as almost completed except some remaining points that needed to be proven experimentally. Or more precisely, people lost the interests in this field largely because the current trend in the community does not look at this class of materials as an interesting candidate anymore. However, this does not mean that the physics in this is all lost. There are still a lot of mysteries to solve with other class of materials such as the ones discussed in this thesis. Especially for the ones that our current technologies vastly adopted and already

started using even without deeper understandings. As usual, more profound understandings could open new possibilities such as in the case of silicon industry - started with the discovery of a transistor but truly flourished after deeper understanding of materials and physics behind them were fully established, and new class of devices were emerged based on these. I believe strongly that the strongly correlated systems such as magnetic materials are currently going through the same phase now. Their technical appications have been vastly increased over past two decades despite of the lack of understanding the physcis behind them. Which is why more and more people are drawn into this field. This is where previous researches in normal metals become important because it will provide us a good solid starting point. I believe my research could serve such a purpose in this growing field of nanoscale electronics with strongly correlated systems.

References

[1] F. Walz, "The Verwey transition - a topical review," J. Phys.: Condens. Matter **14**, R285–R340 (2002).

[2] A. J. Trionfi, *Electron phase coherence in mesoscopic normal metal wires*, Ph.D. thesis, Rice University (2006).

[3] Stephen Blundell, *Magnetism in Condensed Matter* (Oxford University Press, 2006).

[4] R. M. Bozorth, *Ferromagnetism* (Wiley - IEEE Press, 1993).

[5] R. C. Jaklevic, J. Lambe, A. H. Silver, and J. E. Mercereau, "Quantum interference effects in Josephson tunneling," Phys. Rev. Lett. **12**, 159–160 (1964).

[6] S. Lee, A. Trionfi, and D. Natelson, "Quantum coherence in a ferromagnetic metal: time-dependent conductance fluctuations," Phys. Rev. B **70**, 212407–212410 (2004).

[7] S. Lee, A. Trionfi, T. Schallenberg, H. Munekata, and D. Natelson, "Mesoscopic conductance effects in InMnAs structures," Appl. Phys. Lett. **90**, 032105–032107 (2007).

[8] S. Lee, A. Fursina, J. T. Mayo, C. T. Tavuz, V. L. Colvin, I. V. Shvets, and D. Natelson, "Electrically-driven phase transition in magnetite nanostructures," Submitted to Nature Materials in 2007.

[9] Neil W. Ashcroft and N. David Mermin, *Solid State Physics* (Saunders College Publishing, 1976).

[10] Charles Kittel, *Introduction to Solid State Physics* (Wiley Interscience Publication, New York, 1996).

[11] Toru Moriya, *Spin Fluctuations in Itinerant Electron Magnetism* (Springer-Berlag, 1985).

[12] David Jiles, *Introduction to Magnetism and Magnetic Materials* (Chapman and Hall, London, 1991).

[13] R. C. O'Handley, *Modern magnetic materials* (Wiley Interscience Publication, New York, 2000).

[14] Alex Goldman, *Handbook of Modern Ferromagnetic Materials* (Kluwer Academic Publishers, 1999).

[15] J. Briaire, *1/f noise in permalloy*, Ph.D. thesis, Eindhoven University of Technology (2000).

[16] K. Honda and S. Kaya, Sci. Rep. Tohoku Imp. Univ. **15**, 721 (1926).

[17] T. McGuire and R. Potter, "Anisotropic magnetoresistance in ferromagnetic 3d alloys," IEEE Trans. on Magn. **11**, 1018–1038 (1975).

[18] Y. Iye, A. Oiwa, A. Endo, S. Katsumoto, F. Matsukura, A. Shen, H. Ohno, and H. Munekata, "Metal-insulator transition and magnetotransport in III-V compound diluted magnetic semiconductors," Mater. Sci. Engineer. B **63**, 88–95 (1999).

[19] H. Munekata, H. Ohno, S. von Molnar, A. Segmuller, L. L. Chang, and L. Esaki, "Metal-insulator transition and magnetotransport in III-V compound diluted magnetic semiconductors," Phys. Rev. Lett. **63**, 1849–1852 (1989).

[20] H. Munekata, H. Ohno, R. R. Ruf, R. J. Gambino, and L. L. Chang, "P-Type diluted magnetic III-V semiconductors," J. Cryst. Growth **11**, 1011–1015 (1991).

[21] M. Conath and W. Nolting, eds., *Local-Monent Ferromagnets* (Springer-Verlag, Heidelberg, 2005).

[22] F. Matsukura, A. Shen, H. Ohno, and Y. Sugawara, "Transport properties and origin of ferromagnetism in (Ga,Mn)As," Phys. Rev. B **57**, R2037–R2040 (1998).

[23] H. Akai, "Ferromagnetism and Its Stability in the Diluted Magnetic Semiconductor (In, Mn)As," Phys. Rev. Lett. **81**, 3002–3005 (1998).

[24] E. J. W. Verwey, "Electronic conduction in magnetite (Fe_3O_4 and its transition point at low temperatures," Nature **144**, 327–328 (1939).

[25] R. W. Millar, "The heat capacitise of low temperatures of "ferrous oxide," magnetite and cuprous and cupric oxides," J. Am. Chem. Soc. **51**, 215–222 (1929).

[26] L. R. Bickford Jr., "The Low Temperature Transformation in Ferrites," Rev. Mod. Phys. **25**, 75–79 (1953).

[27] F. Walz and H. Kronmüller, "Analysis of Magnetic Point-Defect Relaxations in Electron-Irradiated Magnetite," Phys. Status Solidi (b) **181**, 485–498 (1994).

[28] C. Schönenberger, "Introduction to mesoscopic physcis I," Lecture notes.

[29] B. L. Altshuler and A. G. Aronov, *Electron-electron interactions in disordered conductors*.

[30] S. Kasai, T. Niiyama, E. Saitoh, and H. Miyajima, "Aharonov-Bohm oscillation of resistance observed in a ferromagnetic Fe-Ni nanoring," Appl. Phys. Lett. **81**, 316–318 (2002).

[31] G. Tatara, H. Kohno, E. Bonet, and B. Barbara, "Aharonov-Bohm oscillation in a ferromagnetic ring," Phys. Rev. B **69**, 054420–054424 (2004).

[32] S. Kogan, *Electronic noise and fluctuations in solids* (Cambridge University Press, New York, 1996).

[33] P. Dutta and P. M. Horn, "Low frequency fluctuations in solids: $1/f$ noise," Rev. Mod. Phys. **53**, 497–516 (1981).

[34] B. L. Altshuler, P. A. Lee, and R. A. Webb, eds., *Mesoscopic Phenomena in Solids* (North-Holland Press, 1991).

[35] P. J. McConville, *A Quantitative Test of Quantum Transport in Ag Films*, Ph.D. thesis, Michigan State University (1995).

[36] D. Hoadley, P. McConville, and N. O. Birge, "Experimental comparison of the phase-breaking lengths in weak localization and universal conductance fluctuations," Phys. Rev. B **60**, 5617–5625 (1999).

[37] P. A. Lee and A. D. Stone, "Universal conductance fluctuations in metals," Phys. Rev. Lett. **55**, 1622–1625 (1985).

[38] P. A. Lee, A. D. Stone, and H. Fukuyama, "Universal conductance fluctuations in metals: Effects of finite temperature, interactions, and magnetic field," Phys. Rev. B **35**, 1039–1070 (1987).

[39] D. J. Thouless, "Maximum metallic resistance in thin wires," Phys. Rev. Lett. **39**, 1167–1169 (1977).

[40] S. Feng, P. A. Lee, and A. D. Stone, "Sensitivity of the conductance of a disordered metal to the motion of a single atom: implications for $1/f$ noise," Phys. Rev. Lett. **56**, 1960–1963 (1986).

[41] S. Feng, P. A. Lee, and A. D. Stone, "Erratum: Sensitivity of the conductance of a disordered metal to the motion of a single atom: implications for $1/f$ Noise," Phys. Rev. Lett. **56**, 2772 (1986).

[42] A. D. Stone, "Reduction of low-frequency noise in metals by a magnetic field: Observability of the transition between random-matrix ensembles," Phys. Rev. B **39**, 10736–10743 (1989).

[43] B. L. Altshuler and B. Z. Spivak, "Variation of the random potential and the conductivity of samples of small dimensions," JETP lett. **42**, 447–450 (1985).

[44] A. Trionfi, S. Lee, and D. Natelson, "Electronic coherence in metals: comparing weak localization and time-dependent conductance fluctuations," Phys. Rev. B **70**, 041304–041307 (2004).

[45] K. Hong and N. Giordano, "Approach to mesoscopic magnetic measurements," Phys. Rev. B **51**, 9855–9862 (1995).

[46] G. Tatara and H. Fukuyama, "Resistivity due to a Domain Wall in Ferromagnetic Metal," Phys. Rev. Lett. **78**, 3773–3776 (1997).

[47] V. K. Dugaev, P. Bruno, and J. Barnas, "Weak localization in ferromagnets with spin-orbit interaction," Phys. Rev. B **64**, 144423 (2001).

[48] S. Adam, M. Kindermann, S. Rahav, and P. W. Brouwer, "Mesoscopic anisotropic magnetoconductance fluctuations in ferromagnets," Phys. Rev. B **73**, 212408–212411 (2006).

[49] M. Aprili, J. Lesueur, L. Dumoulin, and P. Nedellec, "Weak localization and electron-electron interaction in percolating nickel films," Solid State Commun. **102**, 41–46 (1997).

[50] S. Kasai, E. Saitoh, and H. Miyajima, "Quantum transport properties in ferromagnetic nanorings at low temperature," J. Appl. Phys. **93**, 8427–8429 (2003).

[51] L. Vila, R. Giraud, L. Thevenard, A. Lemaitre, F. Pierre, J. Dufouleur, D. Mailly, B. Barbara, and G. Faini, "Mesoscopic Resistance Fluctuations in Cobalt Nanoparticles," Phys. Rev. Lett. **98**, 027204–027207 (2007).

[52] T. Schallenberg and H. Munekata, "Preparation of ferromagnetic (In,Mn)As with a high Curie temperature of 90 K," Appl. Phys. Lett. **89**, 042507–042509 (2006).

[53] J. H. Scofield, "ac method for measuring low-frequency resistance fluctuation spectra," Rev. Sci. Instr. **58**, 985–993 (1987).

[54] Th. G. S. M. Rijks, S. K. J. Lenczowski, R. Coehoom, and W. L. M. de Jonge, "In-plane and out-of-plane anisotropic magnetoresistance in $Ni_{80}Fe_{20}$ thin films," Phys. Rev. B **56**, 362–366 (1997).

[55] B. L. Altshuler, A. G. Aronov, and P. A. Lee, "Interaction effects in disordered Fermi systems in two dimensions," Phys. Rev. Lett. **44**, 1288–1291 (1980).

[56] K. Miyake, K. Shigeto, K. Mibu, T. Shinjo, and T. Ono, "Geometrical confinement of a domain wall in a nanocontact between two NiFe wires," J. Appl. Phys. **91**, 3468–3470 (2002).

[57] P. Esquinzi, ed., *Tunneling systems in amorphous and crystalline solids* (Springer, New York, 1998).

[58] N. O. Birge, B. Golding, and W. H. Haemmerle, "Electron quantum interference and $1/f$ noise in bismuth," Phys. Rev. Lett. **62**, 195–198 (1989).

[59] N. O. Birge, B. Golding, and W. H. Haemmerle, "Conductance fluctuations and $1/f$ noise in Bi," Phys. Rev. B **42**, 2735–2743 (1990).

[60] N. E. Israeloff, M. B. Weissman, G. J. nieuwenhuys, and J. Kosiorowska, "Electrical noise from spin fluctuations in CuMn," Phys. Rev. Lett. **63**, 794–797 (1989).

[61] G. Neuttiens, C. Strunk, C. van Haesendonck, and Y. Bruynseraede, "Universal conductance fluctuations and low-temperature $1/f$ noise in mesoscopic AuFe spin glasses," Phys. Rev. B **62**, 3905–3909 (2000).

[62] Y. Koyama and Y. Takane, "Quantum Interference Effect on the Conductance of a Ferromagnetic Wire with a Domain Wall," J. Phys. Soc. Jpn. **72**, 634–644 (2003).

[63] J. Jaroszyński, J. Wróbel, M. Sawicki, E. Kamińska, T. Skóskiewicz, G. Karczewski, T. Wojtowicz, A. Piotrowska, J. Kossut, and T. Dietl, "Influence of $s-d$ Exchange Interaction on Universal Conductance Fluctuations in $Cd_{1-x}Mn_xTe$:In," Phys. Rev. Lett. **75**, 3170–3173 (1995).

[64] T. Dietl, H. Ohno, and F. Matsukura, "Hole-mediated ferromagnetism in tetrahedrally coordinated semiconductors," Phys. Rev. B **63**, 195205–195226 (2003).

[65] J. Garciá and G. Subías, "The Verwey transition - a new perspective," J. Phys.: Condens. Matter **16**, R145–R178 (2004).

[66] G. K. Rosenberg, M. P. Pasternak, W. M. Xu, Y. Amiel, M. Hanfland, M. Amboage, R. D. Taylor, , and R. Jeanloz, "Origin of the Verwey transition in magnetite," Phys. Rev. Lett. **96**, 045705–1–045705– (2006).

[67] P. Piekarz, K. Parlinksi, and A. M. Oleś, "Mechanism of the Verwey transition in magnetite," Phys. Rev. Lett. **97**, 156402–1–156402– (2006).

[68] W. W. Yu, J. C. Falkner, C. T. Yavuz, and V. L. Colvin, "Synthesis of monodisperse iron oxide nanocrystals by thermal decomposition of iron carboxylate salts," Chem. Commun. **2004**, 2306–2307 (2004).

[69] Y. Zhou, X. Jin, and I. V. Shvets, "Enhancement of the magnetization saturation in magnetite (100) epitaxial films by thermo-chemical treatment," J. Appl. Phys. **95**, 7357–7359 (2004).

[70] J. Chen, M. A. Reed, A. M. Rawlett, and J. M. Tour, "Large On-Off Ratios and Negative Differential Resistance in a Molecular Electronic Device," Science **286**, 1550 (1999).

[71] M. A. Reed, J. Chen, A. M. Rawlett, D. W. Price, and J. M. Tour, "Molecular random access memory cell," Appl. Phys. Lett. **78**, 3735–3737 (2001).

[72] C. Joachim, J. K. Gimzewski, R. R. Schlittler, and C. Chavy, "Electronic transparence of a single C_{60} molecule," Phys. Rev. Lett. **74**, 2102–2105 (1995).

[73] A. Yazdani, D. M. Eigler, and N. D. Lang, "Off-resonance conduction through atomic wires," Science **272**, 1921–1924 (1996).

[74] S. Datta, W. Tian, S. Hong, R. Reifenberger, J. I. Henderson, and C. P. Kubiak, "Current-voltage characteristics of self-assembled monolayers by scanning tunneling microscopy," Phys. Rev. Lett. **79**, 2530–2533 (1997).

[75] B. C. Stipe, M. A. Rezaei, and W. Ho, "Single-molecule vibrational spectroscopy and microscopy," Science **280**, 1732–1735 (1998).

[76] Z. J. Donhauser, B. A. Mantooth, K. F. Kelly, L. A. Bumm, J. D. Monnell, J. J. Stapleton, D. W. Price Jr., A. M. Rawlett, D. K. Allara, J. M. Tour, and P. S. Weiss, "Conductance switching in single molecules through conformational changes," Science **292**, 2303–2307 (2001).

[77] G. K. Ramachandran, T. J. Hopson, A. M. Rawlett, L. A. Nagahara, A. Primak, and S. M. Lindsay, "A bond-fluctuation mechanism for stochastic switching in wired molecules," Science **300**, 1413–1416 (2003).

[78] H. Park, A. K. L. Lim, A. P. Alivisatos, J. Park, and P. L. McEuen, "Fabrication of metallic electrodes with nanometer separation by electromigration," Appl. Phys. Lett. **75**, 301–303 (1999).

[79] H. Park, J. Park, A. K. L. Lim, E. H. Anderson, A. P. Alivisatos, and P. L. McEuen, "Nanomechanical oscillations in a single-C_{60} transistor," Nature **407**, 57–60 (2000).

[80] J. Park, A. N. Pasupathy, J. I. Goldsmith, C. Chang, Y. Yaish, J. R. Petta, M. Rinkowski, J. P. Sethna, H. D. Abruña, P. L. McEuen, and D. C. Ralph, "Coulomb blockade and the Kondo effect in single-atom transistors," Nature **417**, 722–725 (2002).

[81] W. Liang, M. P. Shores, M. Bockrath, J. R. Long, and H. Park, "Kondo resonance in a single-molecule transistor," Nature **417**, 725–729 (2002).

[82] L. H. Yu and D. Natelson, "The Kondo effect in C_{60} single molecule transistors," Nano Letters **4**, 79–83 (2004).

[83] L. H. Yu and D. Natelson, "Transport in single-molecule transistors: Kondo physics and negative differential resistance," Nanotechnology **15**, S1–S8 (2004).

[84] L. H. Yu, Z. K. Keane, J. W. Ciszek, L. Cheng, M. P. Stewart, J. M. Tour, and D. Natelson, "Inelastic electron tunneling via molecular vibrations in single-molecule transistors," Phys. Rev. Lett. **93**, 266802–1–266802–4 (2004).

[85] T. Burch, P. P. Craig, C. Hedrick, T. A. Kitchens, J. I. Budnick, J. A. Cannon, M. Lipsicas, and D. Mattis, "Switching in magnetite: a thermally driven magnetic phase transition," Phys. Rev. Lett. **23**, 1444–1447 (1969).

[86] P. J. Freud and A. Z. Hed, "Dynamics of the electric-field-induced conductivity transition in magnetite," Phys. Rev. Lett. **23**, 1440–1443 (1969).

[87] J. Duchene, M. Terraillon, P. Pailly, and G. Adam, "Filamentary conduction in VO_2 coplanar thin-film devices," Appl. Phys. Lett. **19**, 115–117 (1971).

[88] Q. Gu, A. Falk, J. Wu, L. Ouyang, and H. Park, "Current-driven phase oscillation and domain-wall propagation in $W_xV_{1-x}O_2$ nanobeams," Nano Lett. **7**, 363–366 (2007).

[89] A. Salazar, A. Oleaga, A. Wiechec, Z. Tarnawski, and A. Kozlowski, "Thermal diffusivity of $Fe_{3-x}Zn_xO_4$," IEEE Trans. Magn. **40**, 2820–2822 (2007).

[90] H. P. Pinto and S. D. Elliot, "Mechanism of the Verwey transition in magnetite: Jahn-Teller distortion and charge ordering patterns," J. Phys.: Condens. Matter **18**, 10427–10436 (2006).

[91] Y. N. Chiang, O. G. Shevchenko, and R. N. Kolenov, "Manifestation of coherent and spin-dependent effects in the conductance of ferromagnets adjoining a superconductor," Low Temp. Phys. **33**, 314–320 (2007).

[92] Y. Lyanda-Geller, I. L. Aleiner, and P. M. Goldbart, "Domain Walls and Conductivity of Mesoscopic Ferromagnets," Phys. Rev. Lett. **81**, 3215–3218 (1998).

[93] A. Stern, "Berrys phase, motive forces, and mesoscopic conductivity," Phys. Rev. Lett. **68**, 1022–1025 (1992).

[94] I. Leonov, A. N. Antonov, and V. I. Anisimov, "Electronic structure of charge-ordered Fe_3O_4 from calculated optical, magneto-optical Kerr effect, and O K-edge x-ray absorption spectra," Phys. Rev. B **74**, 165117– (2006).

[95] L. V. Gasparov, D. B. Tanner, D. B. Romero, H. Berger, G. Margaritondo, and L. Ferró, "Infrared and Raman studies of the Verwey transition in magnetite," Phys. Rev. B **62**, 7939–7944 (2000).